JGR Solid Earth

RESEARCH ARTICLE
10.1029/2023JB027244

Restoration and Transformation: The Response of Shocked and Oxidized Magnetite to Temperature

Bruno Daniel Leite Mendes[1] and **Agnes Kontny**[1]

[1]Institute of Applied Geosciences—Structural Geology and Tectonics, Karlsruhe Institute of Technology, Karlsruhe, Germany

Key Points:

- Shock-induced lattice defects in magnetite alter magnetic behavior and apparent magnetic domain state; annealing partially restores them
- Hematite in oxidized magnetite transforms back to magnetite with heating. Newly formed magnetite has a SD-SP grain size range
- Using high-resolution FORC analysis, we distinguish between annealing and newly formed magnetite from transformation in heating experiments

Correspondence to:

B. D. L. Mendes,
b.daniel.lm@gmail.com;
bruno.mendes@kit.edu

Citation:

Mendes, B. D. L., & Kontny, A. (2024). Restoration and transformation: The response of shocked and oxidized magnetite to temperature. *Journal of Geophysical Research: Solid Earth*, *129*, e2023JB027244. https://doi.org/10.1029/2023JB027244

Received 7 JUN 2023
Accepted 26 JAN 2024

Author Contributions:

Conceptualization: Bruno Daniel Leite Mendes
Data curation: Bruno Daniel Leite Mendes
Formal analysis: Bruno Daniel Leite Mendes
Investigation: Bruno Daniel Leite Mendes
Methodology: Bruno Daniel Leite Mendes
Project administration: Agnes Kontny
Supervision: Agnes Kontny
Writing – original draft: Bruno Daniel Leite Mendes
Writing – review & editing: Agnes Kontny

Abstract Large impact craters on Earth are associated with prominent magnetic anomalies, residing in magnetite of the shocked target rocks and impactites. Shock experiments on magnetite suggest that up to 90% of magnetic susceptibility is lost at pressures >5 GPa, but can be partially restored by post-shock thermal annealing. The magnetic property changes are caused by shock induced grain size reduction and fragmentation, as well as domain wall-pinning at crystal lattice defects. A recent study of granitoids from the peak-ring of the Chicxulub crater found that annealing may occur naturally, but can also be overprinted by high-temperature hematite-to-magnetite transformation in non-oxidizing environments. In this study, we isolate the effect of defect annealing and hematite-to-magnetite transformation using the evolution of hysteresis, isothermal remanent magnetization components and first order reversal curve (FORC) diagrams at different high-temperature steps. We used a laboratory-shocked magnetite-quartz ore, a non-shocked naturally oxidized granite, and a naturally shocked and oxidized granite. Our findings suggest that annealing of shock-induced lattice defects partially restores some pre-shock magnetic behavior and causes an apparent average bulk-sample domain state increase. Hematite-to-magnetite transformation creates new fine-grained magnetite that strongly overprints the original signal, and decreases the average bulk-sample domain state. Where annealing and hematite-to-magnetite transformation both occur, the new magnetite masks the annealing-induced property restoration and apparent domain state modification in the shocked magnetite. As magnetite oxidation is a ubiquitous process in surface rocks, these findings are fundamental to understand hematite-to-magnetite transformation as a potential overprint mechanism, and could have broad implications for paleomagnetic interpretations.

Plain Language Summary Magnetite is the dominant magnetic mineral in the Earth's crust and is also found in shocked rocks of impact craters, where it can lose up to 90% of its induced magnetization due to fractures and defects in the crystal lattice. Previous experiments in shocked magnetite ore suggest that thermal treatment can recover some shock-induced defects, and even restore some lost magnetic properties. Similar changes in magnetic properties have been observed in non-shocked granites with magnetite and hematite after heating, because in non-oxidizing environments hematite transforms back to very small magnetite grains at high temperatures. Shocked magnetite from the Chicxulub crater is also oxidized to hematite before the impact, and it is unclear if the heating-induced change of magnetic properties is due to the recovery of shock defects, or hematite-to-magnetite transformation. We investigated magnetite from a laboratory-shocked magnetite-quartz ore, a non-shocked naturally oxidized granite, and the granite from Chicxulub at different temperature steps with high-resolution magnetic methods, and delineated the effects of physical and chemical alteration. We find that hematite-to-magnetite transformation overprints the original signal in a similar way to the annealing of shock-induced features. This study is fundamental for discriminating shock and chemical alteration on the magnetic behavior of magnetite.

1. Introduction

Large impact craters on Earth are associated with prominent magnetic anomalies, carried by magnetite in shocked and impact-related rocks (e.g., Gattacceca et al., 2007; Gilder et al., 2018; Hart et al., 1995; Quesnel et al., 2013). In fact, the famous Chicxulub impact crater, associated with the K-Pg boundary and a mass extinction linked to a severe global climate change event (e.g., Hildebrand et al., 1991; Schulte et al., 2010; Sharpton et al., 1992; Smit, 1999), was discovered by Penfield and Camargo (1981) through its aeromagnetic and gravity anomaly. Magnetic anomalies are a result of the displacement of the magnetized rocks in the impact cratering process, decomposition of the existing rock magnetization, and formation of new magnetic phases in impactites (e.g., Hart

et al., 1995; Pilkington & Grieve, 1992; Plado et al., 1999). Although magnetic anomalies in impact craters are well documented, the effect of shock on the magnetic behavior of magnetite has only been studied in detail in the last decade (e.g., Carporzen et al., 2006, 2010; Louzada et al., 2010; Tikoo et al., 2015; Reznik et al., 2016). The shockwave released by an impact causes a nearly instantaneous compression and decompression of the target, and a loss of up to two-thirds of the magnetic moment (e.g., Gilder et al., 2006) and up to 90% of the magnetic susceptibility (Reznik et al., 2016), if magnetite is responsible for the magnetization. Loss of magnetic susceptibility in particular results from brittle fracturing and fragmentation of large grains, and from plastic deformation such as lattice defects or dislocations, that lead to a deformed and strained crystal lattice (Kontny et al., 2018; Reznik et al., 2016).

The magnetic behavior of magnetite is closely related to its grain size and crystal structure. The smallest magnetite grains (<~30 nm, Dunlop, 1973) are superparamagnetic (SP), and are incapable of carrying a NRM. Larger grains have the ability to record a NRM (given by M_{rs}/M_s, where M_s is the saturation magnetization, and M_{rs} is the saturation remanent magnetization), but this ability is also subordinate to grain size and shape. Small grains (<~80 nm for rounded, and <~300 nm for elongated shapes, Newell & Merrill, 1999; Witt et al., 2005) are generally uniformly magnetized in a single domain (SD) state, and are resistant to changes in magnetization (i.e., they have a high coercivity, B_c). With increasing grain size, a single domain becomes unstable and collapses into a circular shape, or "vortex" (V, commonly referred to in literature as pseudo-single domain, PSD; e.g., Roberts et al., 2000, 2017), comprising either a single vortex (SV, see e.g., Pike & Fernandez, 1999) or multiple vortexes (MV), and its coercivity depends on the size, number and shape of the vortexes (Lascu et al., 2018).

For even larger grains, multiple vortexes resolve into multiple discrete domains (MD), separated by narrow so-called domain walls which migrate relatively freely within the grain in response to external magnetic fields. The transition from PSD/V state to MD state has been described to occur in magnetite particles around ~10 μm (Nagy et al., 2019). MD grains have generally low coercivity, due to the relative ease of migration of the domain walls. However, the presence of physical obstacles such as shock-induced fissures and fractures, lattice defects, or dislocation networks, will often "pin" the walls along them, in a process of "domain-wall pinning" (e.g., Lindquist et al., 2015; Moskowitz, 1993; Özdemir & Dunlop, 1997). If a wall becomes pinned it can still migrate, but requires a higher field intensity to do so (manifested as increased coercivity), and will "jump" from one dislocation/defect to the next, in a so called "Barkhausen jump" (Barkhausen, 1919). MD is the most common domain state in natural magnetite, including those from large impact craters, but the associated shock-induced brittle and plastic deformation fundamentally alters these grains, leading to magnetic behaviors more typical of the PSD/V state such as lower magnetic susceptibility, higher coercivity and higher M_{rs}/M_s (Kontny et al., 2018; Reznik et al., 2016).

While brittle fracturing and fragmentation irreversibly reduces grain size, the lattice defects are plastic deformation features that can be annealed through a thermal treatment that reduces wall-pinning (e.g., Pike, Roberts, Dekkers, & Verosub, 2001). Annealing of shocked magnetite leads to a recovery of magnetic susceptibility and a striking irreversibility of temperature dependent magnetic susceptibility (κ-T curves), as well as a decrease in coercivity and M_{rs}/M_s. These changes in magnetic properties lead to an apparent increase in the domain state after heating, toward a more MD-like behavior (Kontny et al., 2018). A recent study on the effects of natural shock and post-impact high temperature exposure on the magnetic behavior of granitoids from the Chicxulub peak ring, reports that defect annealing can occur naturally (Mendes et al., 2023). However, the effects of annealing are often overprinted by the transformation of secondary hematite into newly formed, fine and mottled textured magnetite (Mendes et al., 2023). The κ-T curves of both phenomena show a similar irreversible behavior (Figure 1) with an onset of annealing and/or chemical transformation at ~540°C (Mendes et al., 2023). Standard magnetic methods such as bulk-sample hysteresis or isothermal remanent magnetization component analysis were not sensitive enough to separate magnetic property changes caused by annealing and hematite-to-magnetite (hem-mt) transformations (Mendes et al., 2023). These effects likely overlap in natural impact craters as oxidized magnetite is not only described from Chicxulub (Mendes et al., 2023), but also in Chesapeake Bay (US) (Mang & Kontny, 2013), Vredefort (S-Africa) (Carporzen et al., 2006), Zhamanshin Astrobleme (Kazakhstan) (Sergienko et al., 2021), Manicouagan (Canada) (Morris et al., 1995), Bosumtwi (Ghana) (Kontny et al., 2007), and the Gusev impact crater on Mars (Morris et al., 2006).

In this study, we used hysteresis, isothermal remanent magnetization components analysis and first order reversal curve (FORC) diagrams at different high-temperature steps to investigate systematically each process and their

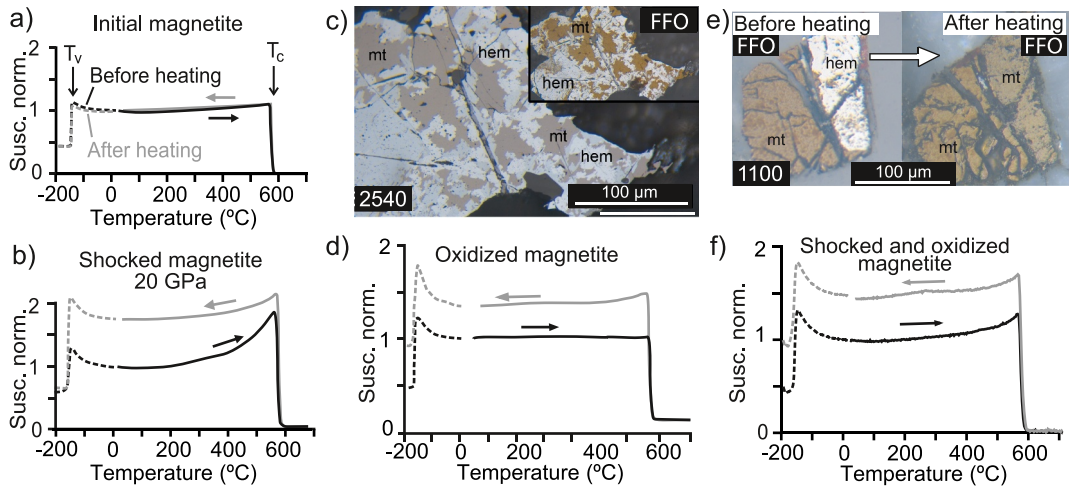

Figure 1. Previous literature data on the response of our samples' temperature treatment. (a) Temperature-dependent magnetic susceptibility (Susc. norm. vs. Temperature) for Initial magnetite ore (after Kontny et al., 2018); (b) Temperature-dependent magnetic susceptibility for magnetite ore shocked at 20 GPa, note the peaks at the Verwey transition and Curie temperature (after Kontny et al., 2018); (c) Strong transformation of magnetite to hematite in sample representative of the Stage-I alteration of the Soultz-sous-Forêts granite, with and without ferrofluid (FFO) for clear contrast (after Just & Kontny, 2012); (d) Normalized temperature dependent susceptibility curve for sample 2,533, which is similar oxidized as sample 2,540 in (c) (Just & Kontny, 2012); (e) Hematite-to-magnetite transformation before (left) and after (right) temperature dependent susceptibility measurement to 700°C in sample 1,100 from the Chicxulub peak ring, with ferrofluid (FFO) for clear contrast (after Mendes et al., 2023); (f) Normalized MS-T curve for the sample represented in (a) is taken from Mendes et al. (2023).

interactions. Specifically, we aim to (a) isolate physical (shock) and chemical (hem-mt transformation) effects on magnetite, (b) observe and characterize the magnetic properties and (apparent or real) domain state and associated magnetic behavior evolution with temperature in shocked and oxidized samples, (c) define an approximate temperature threshold for annealing and hem-mt transformation, (d) determine the dominant phenomenon in complex natural samples such as the shocked Chicxulub basement and its implications for application of magnetic methods in crustal impact structures, and (e) explore the implications of hem-mt transformation for broader rock-magnetic studies, outside of impact research.

2. Materials and Methods

2.1. Materials

We selected a total of nine samples for this study: seven magnetite ore samples shocked at increasing pressures (from a non-shocked "Initial" sample, to 1, 3, 5, 10, 20 and 30 GPa, as the samples will be referred to as, henceforth), and two natural magnetite samples from the non-shocked Soultz-sous-Forêts granite (France) ("Soultz", or Sample 2,533 and 2,476), and from the Chicxulub impact crater peak ring granitoid basement (Mexico) ("Chicxulub", or sample 1,100).

The magnetite ore used for shock experiments originates from a metamorphosed quartz-magnetite banded iron ore of the Sydvaranger mine (Norway), with alternating polycrystalline quartz layers intergrown with cubic magnetite crystals, and bands of polycrystalline magnetite. This magnetite has a sharp Verwey transition (T_v) at −152 ± 2°C and a Curie temperature (T_c) at 578 ± 2°C (Figure 1a). The shocked magnetite ores are from the same shock experiment batches used in the study of Reznik et al. (2016) and Kontny et al. (2018), and none of them contained hematite. The shock experiments were originally commissioned by Reznik et al. (2016) at the Ernst Mach institute (Freiburg, Germany), using a flyer plate that impacts an ARMCO iron container with a disk-shaped target accelerated either by an air gun (1–5 GPa) or high explosives (10–30 GPa) at a given velocity (see Reznik et al., 2016; and for details on the shock reverberation setup see Müller & Hornemann, 1969; Fritz et al., 2011). After applying shock pressures of 5 GPa and above, the shocked samples show a mass susceptibility decrease of up to 90% (see Figure 11b in Reznik et al., 2016), and an increase of T_v to −144°C while T_c remains relatively

stable. κ-T curves in the shocked magnetite ore are irreversible, and after heating to 700°C the originally strong Hopkinson peak (Hopkinson, 1889) decreased (Figure 1b).

Non-shocked granite samples (2,533 and 2,476) with magnetite oxidized to hematite (stage I alteration in Just & Kontny, 2012) comes from the EPS-1 drill core of the Soultz-sous-Forêts Variscan granite pluton (France). The Soultz sample comprises large oxidized magnetite grains (Figure 1c, where sample 2,540 represents stage I alteration, after Just & Kontny, 2012), has a magnetic susceptibility of $\sim 10^{-3}$ SI, shows a T_v of -150 ± 2°C and a T_c of 573 ± 2°C. κ-T curves are irreversible, and after heating to 700°C a much higher magnetic susceptibility indicates the transformation of hematite into magnetite (Figure 1d). Sample 2,476, with similar properties, was used in this study for before-after heating experiments, to get an idea of the natural heterogeneity of granite oxidation.

The naturally shocked granite from the peak-ring of the Chicxulub impact crater was obtained from borehole M0077 A, drilled during the joint International Ocean Drilling Program and International Continental Scientific Drilling Program Expedition 364 (Morgan et al., 2017). Magnetite experienced pre-impact oxidation to hematite (Figure 1e; Mendes et al., 2023), and was subjected to natural shock pressures in the ~16–18 GPa range (as determined by planar deformation features in quartz grains), with slight shock attenuation with increased depth (Feignon et al., 2020). The magnetite is stoichiometric, and the granite displays conspicuously low magnetic susceptibility ($\sim 50 \times 10^{-6}$ SI), resulting from shock demagnetization (Mendes et al., 2023). Sample 1,100, which has been used for this study, shows a T_v of -156 ± 2°C and a T_c of 572 ± 2°C, and the κ-T curve displays a significant increase in magnetic susceptibility and a slight "hump" after heating (Figure 1f).

Our sample selection for the FORC measurements allows us to isolate the effects of shock and oxidation, if measured stepwise up to high temperatures. The initial magnetite ore is an ideal standard, with a reversible κ-T curve and behavior typical of MD magnetite that remains stable with temperature. The remaining magnetite ore samples have only been exposed to increasing shock and contain no evidence of chemical alteration, which provides insights into domain state evolution with increasing shock and annealing. The natural oxidized magnetite from the Soultz granite (2,533) allows us to constrain the effects of the hem-mt transformation with temperature in the absence of shock deformation. Finally, the naturally shocked and oxidized magnetite from the Chicxulub (1,100) peak ring granitoid provides sample where both shock-annealing and oxidation-transformation relationships can be investigated.

2.2. Sample Preparation

We used small magnetite shards from the shocked ore samples Initial, 3 and 5 GPa, and powdered material for the remaining shocked magnetite ore samples (1, 10, 20 and 30 GPa), as they were completely pulverized during the shock experiment. To isolate magnetite in the natural granite samples, we gently crushed the rock and made a magnetic pre-separation using a strong hand-held magnet and a second visual pre-selection of the magnetic grains, to avoid other minerals such as micas. We prepared three additional samples from the granites (1,100, 2,533 and 2,476) for before-after (BA) experiments (see Section 2.3), referred to as "[Sample name] BA", henceforth. Sample mass was measured, and from the powdered shocked magnetite ore and magnetite grains from the granites (which are too small to handle) we created sample-pellets using a high-temperature porcelain-like two-part cement concrete from Omega Engineering, to maintain sample integrity throughout the experiments. Although this cement does not contain iron according to the manufacturer information, traces of iron in this batch cannot be ruled out. Cement impurities or potential unexpected mineral reactions were taken into consideration in the interpretation of the results. The shard samples were placed inside size 4 gel caps, and were immobilized with non-reactive fiber flax wool. Whenever these samples broke or needed extra immobilization, an alumina-silica cement (ZIRCAR Ceramics) was used. The sample pellets were prepared according to the holder size and did not require further immobilization.

2.3. Methods

All experiments were performed at the Institute for Rock Magnetism (IRM, Minneapolis, USA). We used a LakeShore 8,600 Series Vibrating Sample Magnetometer (VSM) instrument with a maximum saturation field of 1 T to measure hysteresis loops, direct current demagnetization (DCD), and FORC acquisition (Pike et al., 1999; Roberts et al., 2000) in sequence for each mass normalized sample, at each temperature step. Samples were heated stepwise using an ASC furnace with a controlled argon (Ar purity of ~99.998%) atmosphere chamber. Each step

began with a flooding of the chamber at a constant argon flow for 10 min, which was then switched to a slower constant flow (~160 mL/min). For the magnetite ore samples, we used 5 steps, at room temperature (RT), 540, 560, 580 and 700°C, while for the natural samples we added the 600 and 650°C steps ("Full-Run" or "FR" experiments). The threshold value of 540°C was used according to the estimated onset of annealing and/or hem-mt transformation reported by Mendes et al. (2023). In the natural samples we performed additional BA experiments, which consisted of a single temperature step up to 700°C. For FR experiments, the desired temperature was held for 15 min, before returning to RT by flowing air around the isolated chamber. For the BA experiments, the maximum temperature was held for 1 hour, to obtain information about the time-dependence of hem-mt transformation. Sample 1,100 BA was exposed to a second 700°C temperature step experiment (held for 15 min) to investigate the stability of the newly formed phase.

Bulk-sample hysteresis parameters were determined from hysteresis loops and DCD curves. Saturation magnetization (M_s), saturation remanent magnetization (M_{rs}), and coercivity (B_c) were estimated from hysteresis single-loop measurements, and coercivity of remanence (B_{cr}) was determined from the DCD curves. The DCD curves were also used for IRM component analysis (Robertson & France, 1994), and were processed using the online software MAX UnMix (Maxbauer et al., 2016). IRM component modeling allows us to isolate and track the evolution of the magnetite and hematite components individually with temperature. By isolating the magnetite and hematite contributions in the natural granite samples, it is possible to compare the magnetite properties in the natural and shocked magnetite ore samples. This is not possible to do with bulk-sample parameters, which include also the hematite contribution without distinction. We applied a fixed number of magnetite components (2) to fit each sample, which is required to compensate for a natural skewness and temperature relaxation in natural magnetic particle systems (e.g., Heslop et al., 2004). The component with the highest signal contribution is what we consider our "main" magnetite component. We determined the mean coercivity of remanence of this main magnetite component at each temperature step for all samples (B_h after Maxbauer et al., 2016). We refer to B_h simply as the "coercivity" of the magnetite fraction, and for variations or trends in both bulk (B_c, B_{cr}) or component (B_h) coercivity, we use "coercivity (*s.l.*)" for better readability.

A total of 151 FORCs were collected per heating step, using a saturation field (B_{sat}) of 500 mT. FORC diagrams were processed using the FORCinel software, version 3.08 (Harrison & Feinberg, 2008). The FORC diagrams have a standard range of B_u field from −100 to 80 mT, and a maximum B_c field of 120 mT. Samples 3 and 5 GPa were measured with a lower B_c field (max = 100 mT) in the initial room temperature (RT) measurements. For consistency, we rescaled these diagrams despite there being no data past B_c= 100 mT. Sample 5 GPa broke into two shards after the second step, causing difficulties stabilizing the sample in the holders, so we removed one of the shards and applied a different mass normalization for these steps. We applied a standard smoothing factor of 4 to all diagrams of the magnetite ore, and a smoothing factor of 6 to the natural samples. One exception is the first measurement for sample 1,100, which required a smoothing factor of 10.

To help visualize the changes in the FORC signals, we investigated the variations in the irreversible component (ΔM_{irr}, the magnitude of switching events between reversal fields (B_r)) and reversible ridge (the contribution of particles with coercivity = 0 mT, given by the vertical feature density profile along $B_c = 0$, after Pike, 2003), at RT and after heating to 700°C. We also calculated the horizontal FORC feature density distribution (along $B_u = 0$) at each temperature step, to help visualize the evolution in coercivity of the central peak lobe. Furthermore, we quantified domain state changes with temperature using a procedure introduced by Reznik et al. (2016). First, we applied a binarization algorithm incorporated into the ImageJ software (Figure 2, left and center; Rasband, 1997), and determined the ratio [%] of black pixels within the area within a threshold that constrains all positive FORC contributions above the 0.05 significance level (Figure 2, right; Heslop & Roberts, 2012). The defined area is referred to as "SD-MD signal area" (Reznik et al., 2016), and ignores small intensity or coercivity variations while being representative of global FORC signal changes. Further details on the method can be found in the legend of Figure 2. A similar outcome can be achieved by tracking the variation of the area within the FORC signal-to-noise envelope at each step, which is readily calculated and displayed by FORCinel, however we decided to use the SD-MD area procedure for a direct comparison with the results presented in Reznik et al. (2016).

In Supplemental file 1 the step by step procedure for estimating the SD-MD signal area [%] and further IRM parameters are described. Supplemental files 2–4 contain our data and are available on Mendeley data, at Mendes and Kontny (2023) [Dataset]. Supplemental file 2 contains all FORC diagrams; file 3 all individual IRM models; and file 4 all raw data files.

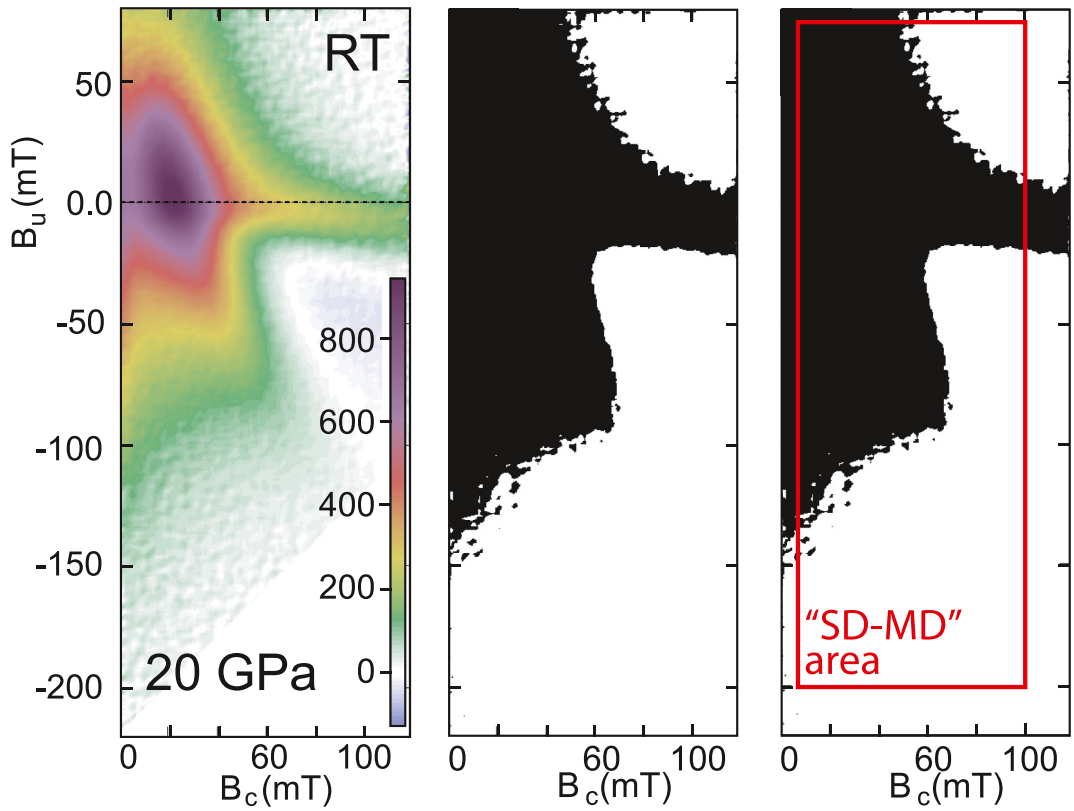

Figure 2. "SD-MD" area calculation scheme, as described by Reznik et al. (2016), using the ImageJ software (Rasband, 1997). We start by importing the original diagram (left), and create a binary black-and-white (BW) version of the diagram (center). Once converted to BW, we select the area defined within the thresholds: $-200 < B_u$ (mT) < 65; and $5 < B_c$(mT) < 100 thresholds (right). This area constrains all positive FORC contributions above the 0.05 significance level (Heslop & Roberts, 2012), and are limited on the bottom and right-hand side to fit the truncated 3 and 5 GPa RT diagrams, as keeping the total diagram area (in pixels) constant, which allows comparisons between samples. The SD-MD area is calculated by the ratio (in percentage) of area covered by the black pixels to the total figure area. Changes in global FORC features with temperature can thus be quantified and compared directly, ignoring subtle intensity or coercivity variations. A detailed step-by-step description is given in supplemental file one; all BW and original FORC diagrams are given in supplemental file 2, together with a calculation sheet for the ratios.

3. Results

3.1. Room Temperature

RT FORC diagrams for the non-shocked Initial magnetite ore (Figure 3a) and Soultz 2,533 (Figure 3b) are typical of MD grains, characterized by a low-coercivity vertical elongation of the FORC signal along the B_c (mT) = 0 axis, and a weak high-coercivity horizontal tail along B_u (mT) = 0. According to IRM component analysis, the Initial magnetite ore shows a coercivity of 13.5 mT (Table 1, RT; Figure 3c). Sample 2,533 shows a slightly higher coercivity of 18.2 mT (Table 1, RT), as well as an additional high-coercivity component, which accounts ~11% to the total signal contribution, which we attribute to hematite (Table 1, green line in Figure 3c). Low shocked (1 and 3 GPa) magnetite ore also retain a MD behavior similar to the non-shocked samples, but with a slightly increased coercivity of 20.1 and 18.2 mT, respectively (Figures 3a and Table 1, RT).

For magnetite ore shocked at 5 GPa, the spread in the spectra of coercivity and interaction field increases strongly compared with lower pressures, but the characteristic closed-contour lobed distributions observed for V-state particles (e.g., Egli, 2021; Lascu et al., 2018; Pike & Fernandez, 1999) are not yet well defined. The sample also denotes an increased coercivity of 33.2 mT (Table 1, RT), which we attribute to a mixture of MD and coarse MV (behaving) grains (e.g., Harrison et al., 2018; Lascu et al., 2018; Roberts et al., 2017). The high shocked magnetite ore at 10, 20, and 30 GPa displays an asymmetric MV-state FORC signal (see e.g., Lascu et al., 2018), with intense closed-contour peak lobe shape and broad horizontal and vertical dispersion. These samples show

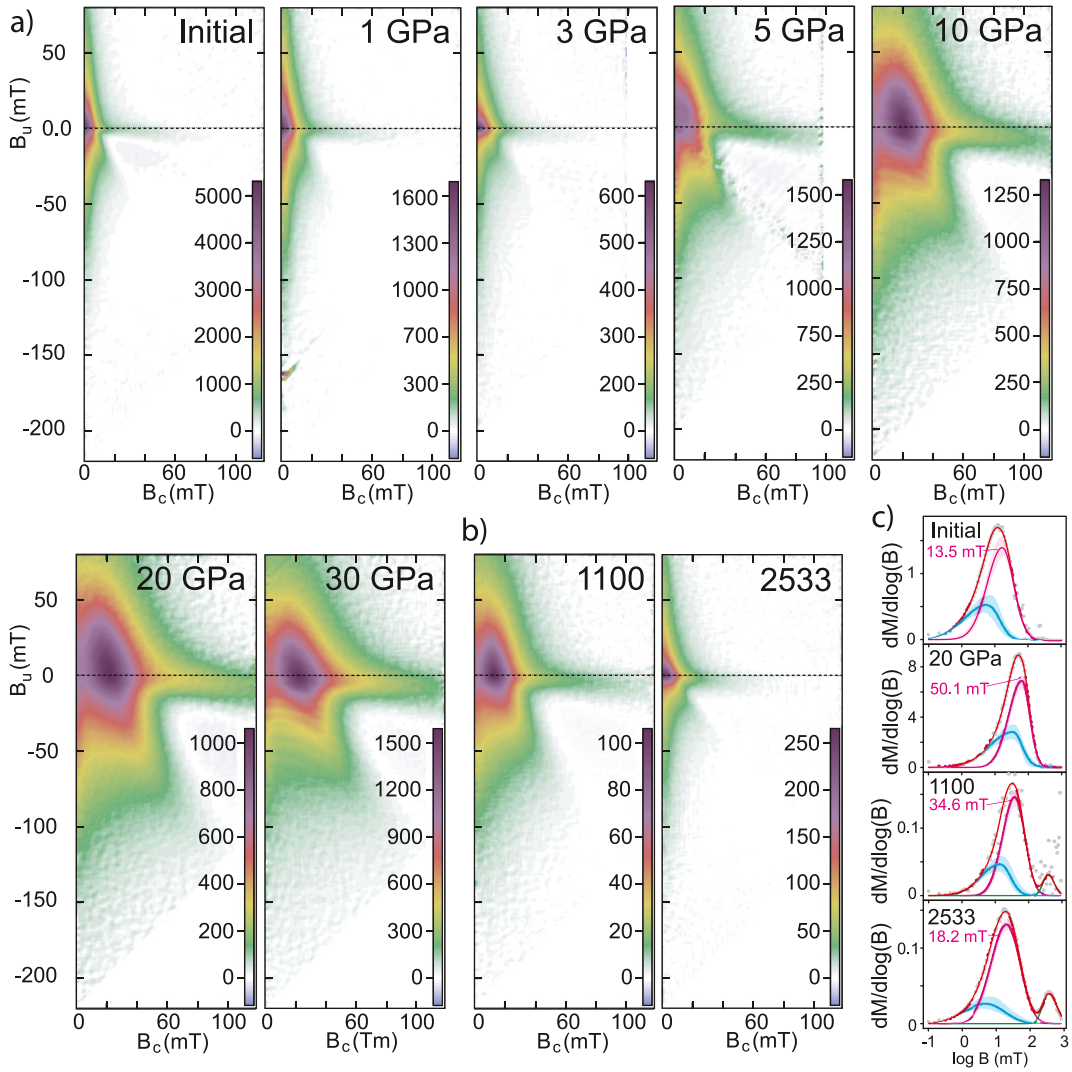

Figure 3. (a) Room-temperature FORC diagrams of all magnetite ore samples before heating. Note the marked development of the PSD/MV lobes in the FORC diagrams with increasing shock pressures ≥5 GPa; (b) Room-temperature FORC diagrams of the natural granite samples, from Chicxulub (1,100) and Soultz (2,533). We used here sample 1100 BA, due to increased measurement noise on the full run sample); (c) Fit of coercivity components to the IRM acquisition curves for representative samples. Note the migration of the components to higher coercivity values between Initial and after 20 GPa shock pressures; note also the presence of a second component (green) in the natural granite samples. Color scale units are in Am^2/kgT^2.

even more increased coercivity values, ranging from 42.3 to 50.1 mT (Table 1, RT), consistent with an increased contribution of MV (and MV-behaving) grains. The vertically elongated signal at low-coercivity is faintly observable around the origin, which suggests that a small amount of grains may have preserved MD behavior (Figure 3a). The Chicxulub sample 1,100 has a similar MV-like lobed distribution signal (Figure 3b), but lower coercivity (34.6 mT) than the high shocked magnetite ore (Table 1, RT; Figure 3c). Note that all FORC distributions at RT in samples shocked above 5 GPa are significantly asymmetric, between the positive and negative values of B_u (Figure 3).

3.2. Temperature-Dependent Measurements

3.2.1. Shocked Magnetite Ore

FORC signals for no and low shocked magnetite ore do not show any variations with temperature. Coercivity decreases slightly after heating in the low shocked magnetite ore (−0.3 mT and −5.8 mT for 1 and 3 GPa,

Table 1
(Top) Mean Coercivity of Remanence (B_h) of the Grain Population of the Main Magnetite Component 1 (Bottom) Total Magnetite (Mt) and Hematite (Hem) Contribution to the Signal With Temperature, in the Natural Granites From Soultz (2,533) and Chicxulub (1,100)

	Average grain population coercvity (Bh) [mT]							
Sample	RT	540°C	560°C	580°C	600°C	650°C	700°C	ΔBh [mT]
Ini	13.5	14.3	13.4	8.1	-	-	12.5	−0.9
1 GPa	20.1	18.1	18.3	16.2	-	-	19.9	−0.3
3 GPa	18.2	12.8	13.4	16.1	-	-	12.3	−5.8
5 GPa	33.2	29.8	21.4	19.5	-	-	18.1	−15.2
10 GPa	42.3	32.4	31.1	30.5	-	-	30.3	−12.0
20 GPa	50.1	36.9	36.3	35.7	-	-	32.4	−17.7
30 GPa	47.6	35.1	34.2	31.1	-	-	30.5	−17.1
1,100 (Chicx)	34.6	38.2	41.9	43.7	47.6	52.3	51.7	+17.2
2,533 (Soultz)	18.2	23.2	28.9	35.1	39.9	43.5	43.2	+25.0
	Contribution to signal [%]							
Sample	RT	540°C	560°C	580°C	600°C	650°C	700°C	
1,100 mt	92.9	95.9	96.4	96.8	98.1	98.6	100.0	
1,100 hem	7.1	4.1	3.6	3.2	1.9	1.4	0.0	
2,533 mt	89.3	92.6	93.1	93.8	94.5	95.3	96.9	
2,533 hem	10.7	7.4	6.9	6.2	5.5	4.7	3.1	

Note. Further IRM modeling parameters can be found in Supplemental file 3.

respectively; Table 1, ΔB_h is the difference between B_h at 700°C and RT). This indicates that MD behavior has not changed with heating (see supplemental file 2 for all FORC diagrams).

For magnetite ore shocked above 5 GPa, we observe a systematic shift of the FORC lobes toward lower coercivity with increasing temperature, and a noticeable decrease in FORC asymmetry (Figure 4a, supplemental file 2). This shift is accompanied by a consistent coercivity decrease with each temperature step, causing ΔB_h in the range from −12.0 mT to −17.7 mT (Table 1). With temperature, the irreversible component (ΔM_{irr}) decreases (see vertical arrows in Figure 4a, top), and the reversible ridge increases (Figure 4a, bottom, also seen in the FORC density plot in Figure 5a). The FORC central peak lobe denotes a clear (leftward) progression toward lower B_c values with temperature (Figure 5a), which is not observable in the no and low shocked magnetite ore (cf. dashed lines and horizontal arrow in Initial and 20 GPa magnetite ore of Figure 5a). The decrease in FORC asymmetry and shift of its features toward lower coercivity result in a systematic decrease in the SD-MD signal area, with a reduction of 10%–15% (downward vertical arrows, Figure 5b). Plotting the hysteresis parameters in a M_{rs}/M_s versus B_{cr}/B_c diagram (Figure 6) highlights the evolution of the magnetic behavior: a shock-induced increase of M_{rs}/M_s and decrease of B_{cr}/B_c, from no and low shocked to high shocked (>5 GPa) magnetite ore (cf. stars in Figure 6) is followed by a systematic decrease of M_{rs}/M_s and an increase of B_{cr}/B_c at each temperature step in the high shocked samples (cf. circles and squares in Figure 6).

3.2.2. Oxidized Magnetite From the Soultz Granite

The evolution of the oxidized Soultz 2,533 granite sample with temperature is divided into two stages: (a) up to 560°C magnetic properties change mildly, while (b) above 560°C changes are much more drastic between each step (Figure 4b).

The first stage up to 560°C, is characterized by a slight strengthening of the horizontal high-coercivity tail (Figure 4b), a reduction of the hematite contribution to the IRM signal from 10.7% to 6.9%, and an increase in the coercivity of magnetite from 18.2 to 28.9 mT (Table 1), suggesting that some hem-mt transformation takes place. At this stage, the central peak lobe does not denote coercivity changes (Figure 5a), the SD-MD signal area remains

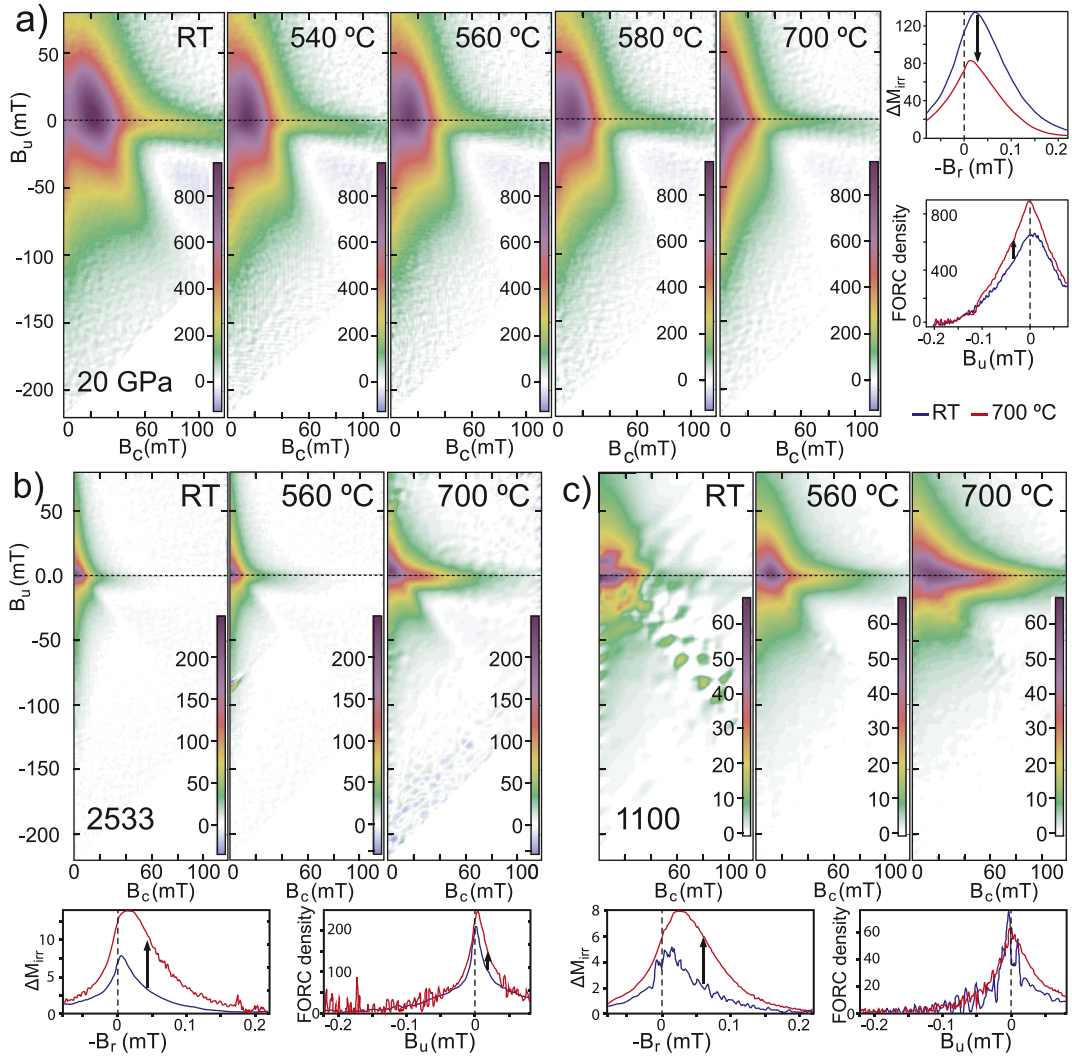

Figure 4. FORC diagrams, vertical FORC density profile for $B_c = 0$ mT (reversible ridge) and irreversible component (given by ΔM_{irr}), that illustrate sample evolution with temperature. (a) Temperature evolution of representative shocked magnetite ore at 20 GPa, which is representative of the high shocked samples; (b) evolution of first and second stages of the hem-mt transformation in sample Soutlz 2,533; and (c) evolution of first and second stages of the Hem-Mt transformation and shock defect annealing in sample Chicxulub 1,100. Scale units are in Am^2/kgT^2 for FORC diagrams and ΔM_{irr}. No and low shocked samples have no FORC signal changes. Results for all other samples can be found in supplemental file 2.

<5%, similar to the no and low shocked magnetite ore (Figure 5b). Only a slight increase in M_{rs}/M_s values at 560° C (Figure 6) is observed, but MD behavior is broadly preserved.

In the second stage above 560°C, the high-coercivity tail grows in intensity, creating a high-coercivity central-ridge like feature in the FORC diagram and a 45° ridge-like feature in the negative interaction field (Figure 4b). The reversible ridge and irreversible component also increase after 700°C (Figure 4b). The formation of the central ridge is observed to accelerate after 600°C (Figure 5a, vertical arrows in Oxidized (2,533)), consistent with a transformation of the hematite component (3.1% after 700°C, Table 1), which causes an increase of the total coercivity in the magnetite fraction, to 43.2 mT (ΔB_h = +25.0 mT). Central peak coercivity remains consistent throughout the experiment, meaning that no changes to the original MD magnetite are taking place (cf. dashed lines in Figure 5a). The SD-MD signal area shows an increase to 12% (Figure 5b), and the sample denotes a strong increase of M_{rs}/M_s and decrease of B_{cr}/B_c after 700°C (Figure 6). As no changes to the MD magnetite fraction are taking place, magnetic property variations are necessarily related to a new magnetite fraction, formed through hem-mt transformation.

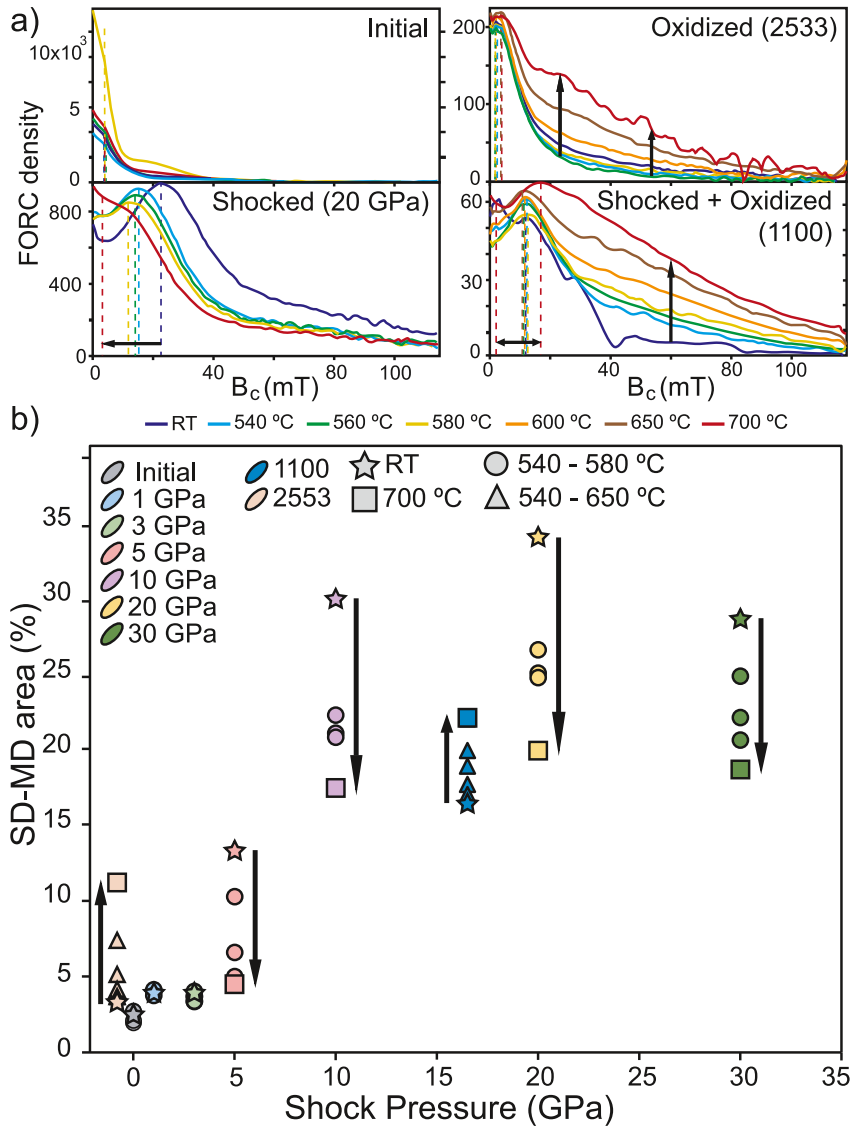

Figure 5. Evolution and variation of the FORC signal with temperature. (a) Horizontal FORC density profiles along the $B_u = 0$ mT axis (i.e., horizontal dashed lines in Figures 3 and 4), at different temperatures, for representative samples of no and low shocked magnetite ore (Initial) and high shocked magnetite ore (20 GPa), as well as both natural granites (2,533 from Soultz and 1,100 from Chicxulub); (b) SD-MD signal area for all investigated samples. Shock pressure of 16.5 GPa for sample 1,100 is an approximation (Feignon et al., 2020). Samples that suffered no shock are plotted for clarity at −1 (sample 2,533) and 0 (Initial magnetite ore). Data of SD-MD area calculations are provided in supplemental file 1 and supplemental file 2, respectively.

3.2.3. Shocked and Oxidized Magnetite From the Chicxulub Granite

The RT FORC of the Chicxulub 1,100 "FR" granite has a noisy signal (see Figure 4c), however the RT measurement for 1,100 BA (used in Figure 3b) allows us to infer an initial asymmetric MV-state FORC diagram, with closed-contour peak lobes similar to the high shocked magnetite ore. The magnetic response to temperature shows now features observed in both the shocked and annealed magnetite ore, and the oxidized and transformed magnetite from the Soultz granite.

Pertaining to the oxidation-related features, Chicxulub 1,100 follows the same two-stage evolution described for Soultz 2,533, up to and above 560°C. In the first stage up to 560°C, the high-coercivity tail becomes more prominent but no central ridge is formed (Figures 4c and 5a), around half of the hematite signal contribution disappears (from 7.1% to 3.6%), and magnetite coercivity increases from 34.6 to 41.9 mT (Table 1). The SD-MD

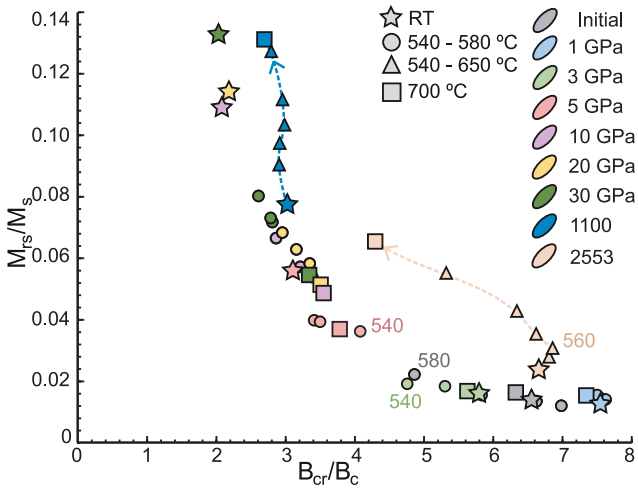

Figure 6. M_{rs}/M_s versus B_{cr}/B_c diagram for all samples at room temperature (RT) and with temperature. Note that shocked magnetite ore at RT shows PSD/V domain state behavior, which moves toward a more MD behavior with increasing temperature. Only oxidized (2,553) and shocked and oxidized (1,100) granite show the contrary trend, with bulk-sample average magnetic domain state decreasing, with increasing temperature (marked by a dashed line and arrows). Numbers mark outliers in samples Initial, 3 and 5 GPa, and the "threshold" of stage 1 and stage 2 of Hem-Mt transformation in sample 2,533.

area largely remains constant, at around 16% (Figure 5b). In the second stage, the central ridge forms (Figure 4c, vertical arrow in Figure 5a), the hematite contribution disappears entirely, and the coercivity of the magnetite fraction increases to 51.7 mT ($\Delta B_h = +17.2$ mT, Table 1). A 45° ridge-like feature in the negative interaction field identical to the one in Soultz 2,533 appears (cf. Figures 4b and 4c), and an increase of the reversible ridge and irreversible component takes place (vertical arrows in Figure 4c). The changes in the FORC features and formation of the central-ridge causes the SD-MD signal area to increase to around 23% at 700°C (Figure 5b). The evolution in the M_{rs}/M_s, versus B_{cr}/B_c diagram does not follow the same pattern as Soultz 2,533, but instead a continuous increase of M_{rs}/M_s and a generally constant B_{cr}/B_c is observed (Figure 6).

The shock-related response in this sample is not as distinct as in the high shocked magnetite ore, but is seen in the FORC diagrams as a shift of the central peak toward lower coercivity (cf. lobe shift in Figure 5a, with elongation of color contours toward the origin in Figure 4c). This shift and the decrease in asymmetry are masked by the formation of the central-ridge, but we can still observe a (leftward) progression of the central peak in the horizontal FORC density profile (Figure 5a). Despite the noisy signal at RT, the density of FORC features at low coercivity increases consistently with temperature (Figure 5a, see the region left of the vertical dashed lines), and culminate in the separation of two peaks at 700°C, one at lower and one at higher coercivity compared to the RT peak (horizontal arrows pointing toward red lines in Figure 5a). The low-coercivity peak has identical coercivity as the Initial, 2,533, and post-heated 20 GPa peaks (cf. red dashed lines of Figure 5a).

3.3. Time-Dependence and Phase Stability

Before heating, 2,533 BA shows a typical MD FORC signal, with a magnetite coercivity of 20.8 mT, and a hematite component with 13.9% signal contribution (Figure 7a, Table 2). After heating, we observe a sharp increase in the intensity and the formation of the central ridge, together with a (rightward) shift of the central FORC feature peak to higher coercivity values in the horizontal profile (vertical and horizontal arrows in Figure 7a). The total disappearance of the hematite component is achieved (Table 2), as the coercivity of magnetite increases from 20.8 to 46.8 mT (Table 2). The reversible ridge and irreversible component also increase significantly (vertical arrows in Figure 7a, bottom). In this experiment, the newly formed magnetite doubles the original sample intensity (Figure 7a) and nearly fully overprints the original MD signal. Sample 2,476 shows identical results (see supplemental file 2).

Before heating, sample 1,100 BA displays an asymmetric MV-state FORC lobe distribution, a smaller hematite component than its "FR" counterpart (only 1.8%), and a magnetite coercivity of 30.8 mT (Table 2). After heating, the hematite contribution disappears, the coercivity of the magnetite fraction doubles (to 60.9 mT, Table 2), and the signal becomes dominated by the newly formed central ridge (Figure 7b). The increase in the reversible and irreversible components is clearer than in the 1100 FR (cf. Figures 7b and 4c). In the horizontal profile, two peaks have formed identical to the FR experiment, however both peaks now have lower coercivity than the original (cf. blue and orange horizontal profiles in Figure 7b). A second heating of sample 1,100 BA to 700°C shows only a slight signal intensity increase compared to the first heating (Figure 7b, "After 2").

4. Discussion

4.1. Shocked Magnetite Ore

Hysteresis loops, IRM component analysis, and FORC diagrams of the shocked magnetite ore demonstrate that below the Hugoniot elastic limit of magnetite (~5 GPa, Ahrens & Johnson, 1995) shock does not create significant irreversible magnetic domain state changes, and thermal annealing also has no significant effect.

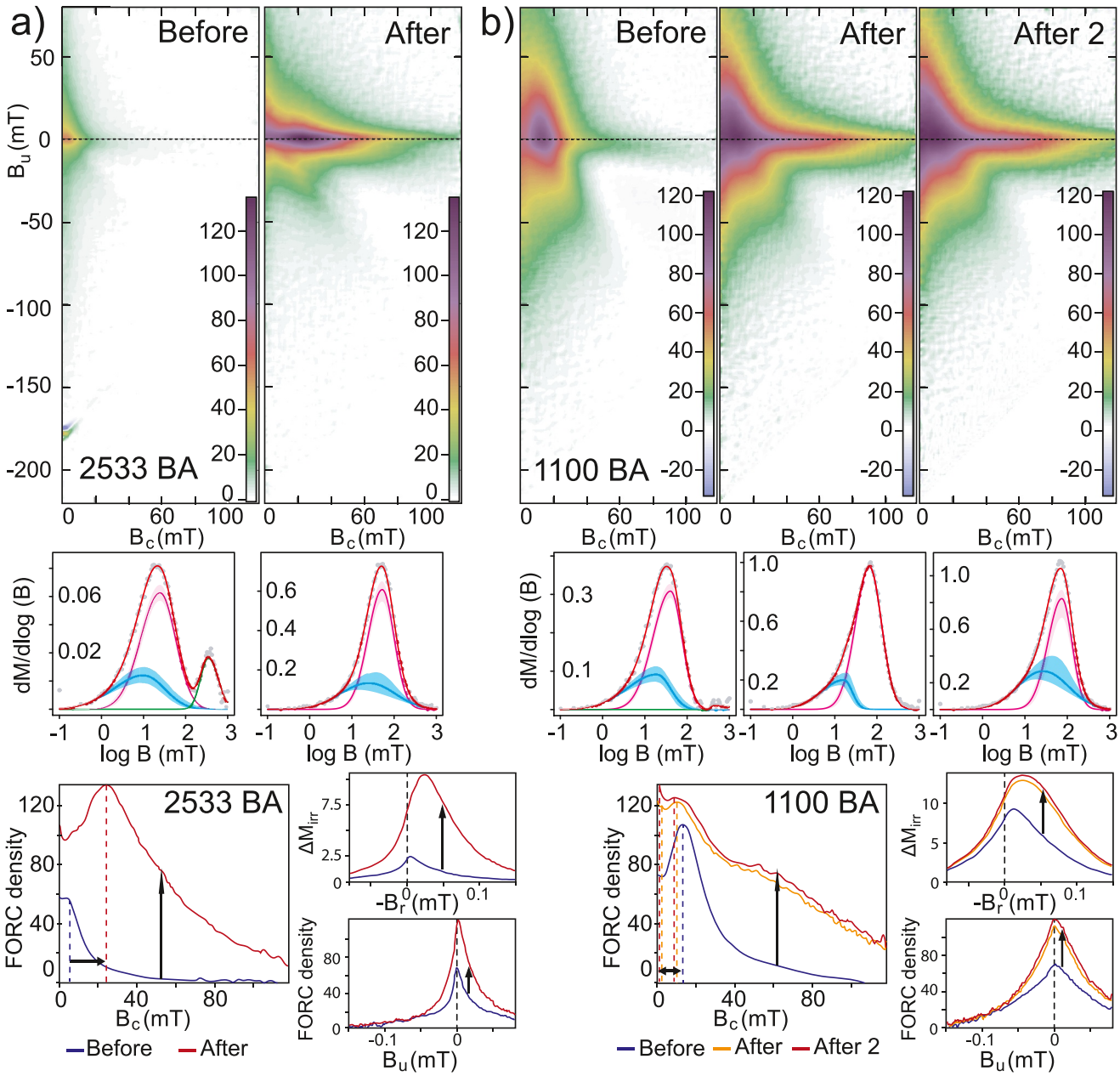

Figure 7. FORC diagrams, fit of coercivity components to the IRM acquisition curves, vertical FORC density profile for $B_c = 0$ mT (reversible ridge) and irreversible component (given by ΔM_{irr}), for the Before-After (BA) experiments in the natural granites. (a) oxidized granite (2,533) from Soultz, note more nearly on order of magnitude intensity increase in the central ridge after heating; (b) shocked and oxidized granite (1,100) from Chicxulub, second measurement "After 2" suggest the newly formed magnetite is stable after repeated heating; see Section 3.3 for details.

In the low shocked magnetite ore, the magnetic characteristics typical for natural undeformed MD magnetite (e.g., by Pike, Roberts, Dekkers, & Verosub, 2001) are largely retained after shock and heating. A slight increase in the magnetite coercivity and M_{rs}/M_s ratios from the Initial to the low-shocked 1 and 3 GPa magnetite ore may indicate a limited increase of domain wall-pinning effects in dislocation networks or local micro-cracks in a strained crystal lattice (Lindquist et al., 2015). Previous studies on MD magnetite at this pressure range are limited to hydrostatic compression experiments between 1 and 4 GPa (see Gilder et al., 2002, 2004, 2006). After decompression, these authors observed a decrease of ~65% in reversible magnetic susceptibility, a slight decrease in the median demagnetization field (field required to demagnetize 50% of the original signal, a proxy for coercivity), and a loss of up to two thirds of magnetic moment. The changes are attributed to a restructuring of domain

Table 2
Mean Coercivity of Remanence (B_h) of Magnetite Before and After Heating to 700°C for Chicxulub (1,100) and Soultz (2,476 and 2,533) Granite, and Signal Contribution of Magnetite and Hematite

	Before			After			After 2		
Sample	Bh [mT]	mt [%]	hem [%]	Bh [mT]	mt [%]	hem [%]	Bh [mT]	mt [%]	hem [%]
1,100 (Chicx)	30.8	98.2	1.8	60.9	100.0	0.0	62.9	100.0	0.0
2,533 (Soultz)	20.8	86.1	13.9	46.8	100.0	0.0	-	-	-
2,476 (Soultz)	18.9	84.4	15.6	37.7	95.1	4.9	-	-	-

Note. Further IRM modeling parameters found in Supplemental file 3.

patterns, increased domain wall nucleation and wall-pinning from an increase in defects. Although a direct comparison of our results with these studies has its limitations (different strain rates between compression-decompression cycles and shock experiments), our results are in agreement with such a model. Gilder et al. (2002, 2004) also noted that magnetic properties only vary slightly below 2 GPa, and become more pronounced between 2 and 3 GPa. The measurements between 2 and 3 GPa were made under pressure thus not directly comparable to ours, however we do observe that annealing at 3 GPa causes a decrease of the magnetite coercivity ($\Delta B_h = -5.8$ mT), whilst at 1 GPa temperature has a negligible effect ($\Delta B_h = -0.6$ mT). The behavior changes are not significant, but the onset of defect annealing leads us to consider that the 3 GPa ore potentially represents a "transitional" stage in shock-deformation.

For magnetite ore shocked at 5 GPa and above, the RT FORC diagrams (Figure 3; stars in Figure 5b), IRM results (Table 1, RT; Figure 3) and hysteresis parameters (stars in Figure 6) demonstrate a trend toward behavior more typical of MV. The lower B_{cr}/B_c and higher M_{rs}/M_s ratios (Figure 6) would also indicate a "PSD" (V) domain state, according to the classical "Day diagram" (Day et al., 1977).

Our FORC results and SD-MD area evolution are similar to observations by Reznik et al. (2016) in different pieces of the same shocked magnetite ore sample material (cf. Figures 3 and 5b of this work, and Figure 9 in Reznik et al., 2016). These features agree well with a transition from a mainly brittle-elastic mechanical behavior at low-shock conditions, toward irreversible brittle-plastic deformation in the higher shocked magnetite ore. In the 5 and 10 GPa magnetite ore, shear bands and particle fragmentation are reported as the dominant microstructural deformation mechanism (Reznik et al., 2016). At 20 GPa, grain fragmentation becomes more intensive, shear bands grow wider and mosaic-like sub-grains form. At 30 GPa, the shockwave leads to the formation of kink-bands, composed of multiple twinned sub-grains (Reznik et al., 2016). The shear- and kink-bands increase the intra-crystalline strain and anisotropy, which is responsible for the distinctly asymmetric FORC signals. The asymmetry of the FORC diagrams can be explained by different vortices created and destroyed at different fields, depending on their location within the crystal (Lascu et al., 2018). With the formation of shear- and kink-bands, the increased strain leads to a widening of the dispersion of the field distribution of the vortex nucleation and annihilation events (Lascu et al., 2018), and thus increasing the asymmetry. While fracturing and fragmentation causes grain size reduction and reduces the bulk-sample average domain state, plastic deformation features create a denser network of physical barriers to domain wall-migration. As domain walls become increasingly pinned along the dense defect network, the expression of individual domains becomes inhibited, resulting in the high M_{rs}/M_s ratios and coercivity (*s.l.*). This leads to magnetic behaviors typical of MV state, despite the magnetite retaining multiple discrete domains, causing an apparent decrease in domain state.

The effects of plastic deformation are partially recovered with temperature, associated with a systematic decrease in magnetite coercivity, FORC asymmetry and SD-MD area, at each step (Table 1, Figures 4a and 5b). Hysteresis parameters also change consistently toward lower M_{rs}/M_s and higher Bcr/B_c ratios, along the classic SD-MD mixing line of Day et al. (1977) toward increased MD contributions (see squares in Figure 6). The increased MD behavior is particularly highlighted by the leftward progression of the FORC central peak toward coercivity values identical to the MD no and low shocked samples (Figure 5a). This suggests that our final results are a composite of MD and MV behaviors, from originally dominant MV behaviors before heating. The partial restoration of the original MD state behavior through temperature is caused by a mosaic-like recrystallization of magnetite, in line with a recovery of lattice defects (Kontny et al., 2018). The defect recovery and recrystallization relaxes the elastic crystal strain, and allows the magnetic domain walls to migrate more easily again. Easier

migration reduces grain coercivity (*s.l.*) and the occurrence of Barkhausen jumps of domain walls, thus reducing the irreversible component, and consequently increasing the reversible ridge (Figure 4a). It also decreases domain wall-nucleation, which increases the individual domain volume size (Kontny et al., 2018). The MV behavior that is preserved after heating derives from the reduced grain size caused by irreversible brittle fracturing and fragmentation.

4.2. Oxidized Magnetite From the Soultz Granite

The disappearance of hematite with temperature in the natural magnetite-bearing granite is clear and systematic, concomitant with the formation of new magnetite grains from hematite-to-magnetite transformation that causes an increase in coercivity of magnetite (Table 1; Figure 4b). The hem-mt transformation process is associated with an increase both in reversible ridge and irreversible components, and the formation of a high coercivity central ridge in the FORC diagrams, which increases the SD-MD signal area (Figures 4b, 5a and 5b).

The formation of the central ridge is fundamental to understand the properties of the newly formed phase, as central ridges are typical for non-interacting SD (e.g., Harrison et al., 2018; Roberts et al., 2019), or SV (Lascu et al., 2018) grains. SV-dominated FORC diagrams have lobes that are confined to the positive and negative interaction fields (e.g., Zhao et al., 2017) and are as intense as the central ridge. A negative "trough" feature immediately below the central ridge is also characteristic of SV grains (Lascu et al., 2018). On the other hand, SD central ridges are much more intense than the remaining features, and do not show the negative "trough" (Lascu et al., 2018). In our granite samples, the intensity of the ridge and lobes is likely dependent on the extent of the hem-mt transformation. Comparing samples 2,533 FR and 2,533 BA (cf. Figures 4b and 7a), the latter has a ridge that is much stronger than the remaining features (cf. Figures 7a and 4b). While the real extent of the hem-mt transformation and amount of newly formed magnetite is hard to estimate (a ∼11% signal contribution of hematite requires its concentration to be much larger than that of magnetite; see Frank & Nowaczyk, 2008; Liu et al., 2019), we can only assume that the transformation in 2,533 BA is more thorough than in 2,533 FR (see contributions in Tables 1 and 2). Therefore, we find it reasonable that given a more complete transformation, the central ridge is significantly stronger than the other contributions (Figure 7a, horizontal profile). Additionally, we do not observe a "trough" feature below the central ridge, which is more in line with a SD state for the newly formed magnetite. The formation of a Hopkinson peak after heating in the κ-T curve for this sample (Figure 1d) supports this interpretation as the Hopkinson peak is a feature associated with the unblocking of SD state just below T_c (Dunlop, 2014). Interaction between the original MD and newly formed SD grains, two fractions of contrasting coercivity, causes the positive area above the 45° ridge in the negative interaction fields. A sharp increase in the irreversible component is well explained by the formation of SD grains, due to an increase in the irreversible rotation of SD magnetization vectors (e.g., Birčáková et al., 2019). As for the reversible ridge, it is unlikely that the increase is caused by changes in domain wall migration, as no fundamental changes to the original MD magnetite take place (Figure 5a). Therefore, the increase must be related to newly formed magnetite, likely a fraction of newly formed SP grains, whose magnetization is entirely reversible (Roberts et al., 2000).

The formation of fine grained SD-SP magnetite causes an increase in bulk-sample coercivity, however the coercivity tail of this newly formed phase extends to at least 120 mT (Figures 5a and 7a), a high value even for fine grain sizes. Such high values may be explained by a strained crystal lattice. Jiang et al. (2016) observed that the crystal structure of nanohematite is often preserved in magnetite formed via reduction through heating, which could be a source for such a lattice strain. Alternatively, we also cannot exclude that the high coercivity (*s.l.*) is connected to the formation of some minor maghemite, as the transformation of magnetite to hematite is reported to occur via maghemite as a metastable phase (e.g., Annersten & Hafner, 1973). If present, this maghemite has an insignificant contribution to the magnetic signal, as our IRM modeling results show no signal that can be related to it.

Our results support the hypothesis postulated by Just and Kontny (2012), and Mendes et al. (2023) that hematite, when heated in an inert argon atmosphere, transforms to magnetite (Figure 1e). We assume that the reason for this mineral reaction are traces of hydrocarbons in the argon gas, despite a high Ar purity (∼99.998%; https://industry.airliquide.us/argon). From our BA experiments, we suggest that the formation of the new magnetite phase is an instantaneous process, and that this phase is stable and will not decay or alter with further heating. Mendes et al. (2023) observed that the newly formed magnetite has a mottled texture resulting from small grain sizes that are not resolvable by reflected light microscopy, which is consistent with the SD-SP range proposed here. Lastly,

we can exclude that the new magnetite grains formed due to impurities in the cement mix, as no new magnetic phase was detected after heating the cemented 1, 10, 20 and 30 GPa magnetite ore. However, we cannot exclude some influence of other minerals such as mica, even in small quantities, in facilitating the hem-mt transformation in the granite.

4.3. Shocked and Oxidized Magnetite From the Chicxulub Granite

The Chicxulub granite show features of annealing and hem-mt transformation, both influencing the evolution of the magnetic behavior. These two effects are confirmed by the formation of two FORC feature density peaks (Figure 5a) after temperature treatment.

The shock-induced MV-like behavior is partially reverted through annealing, in the same process described in Section 4.1 for the shocked magnetite ore, however the concomitant hem-mt transformation nearly fully masks it. Partial restoration of the pre-shock MD behavior results in the low coercivity peak, at an identical coercivity to the high shocked magnetite ore after annealing (cf. 1,100 and 1,120 GPa in Figure 5a). At the same time, the formation of SD-SP magnetite grains from hem-mt transformation is responsible for the formation of the second, higher coercivity peak (Figure 5a). The new fine SD-SP magnetite causes the sample to present a behavior typical of MV state (Figure 6). Bulk-sample coercivity (*s.l.*) increases, and the positive feature above the 45° diagonal ridge in the negative interaction field highlights the coercivity contrast between the annealed MD-MV and newly formed SD-SP fractions. The κ-T curve for sample 1,100 is also in good agreement with SD-SP grain formation (see "hump" below gray arrow in Figure 1f), as such "humps" are suggested to be caused by thermal relaxation of SP particles (Gao et al., 2019; Zhao & Liu, 2010). After heating, the SD-SP grains are dominant and counteract the annealing-induced decrease in coercivity (*s.l.*) and SD-MD area. Whilst the restoration of MD behavior is still observable, the classic bulk-sample hysteresis and IRM modeling methods are not able to distinguish between these two effects. Only FORC diagrams, the most sensitive method to detect small scale domain state changes (e.g., Roberts et al., 2014), can distinguish them.

Our observations are relevant for natural impact crater investigations. Magnetite to hematite oxidation is a ubiquitous product of hydrothermal or meteoric alteration of crustal rocks (e.g., Horton et al., 2006, Horton, Hunk, et al., 2009, Horton, Gibson, et al., 2009), so the post-impact high-temperature exposure in impact craters may cause hem-mt transformation naturally, which overprint the original features. This is observed in the Chicxulub crater, where samples in close contact with impact melt have reversible or nearly reversible κ-T curves, with the exception of the same abovementioned "hump" from SD-SP thermal relaxation (Mendes et al., 2023; Pike, Roberts, & Verosub, 2001). Even at very small percentages, SD-SP grains are able to overprint MD signals, also in non-shocked samples (see e.g., Harrison et al., 2018). Shocked magnetite is already demagnetized, so even the transformation of as low as 1.8% of the signal from hematite will cause a significant overprint (see Figure 7b). Lastly, we believe our results from the natural shocked magnetite validate the models postulated by Reznik et al. (2016) and Kontny et al. (2018), and demonstrate that the laboratory-shock and post-shock annealing experiments are good analogs to the natural system.

4.4. Implications

Magnetite is the most dominant ferrimagnetic mineral in the Earth's crust, and consequently also in large impact craters, where prominent negative magnetic anomalies are related to the shock demagnetization and/or extensive alteration and destruction of the magnetite phases (e.g., Pilkington & Grieve, 1992; Scott et al., 1995). Magnetite oxidation is regarded as a near-equilibrium redox phenomenon where magnetite is altered to hematite by oxidation; but the opposite is also possible, where hematite is reduced by hydrogen or organic matter back to magnetite (e.g., Just & Kontny, 2012). Oches and Banerjee (1996) described a hem-mt transformation in oxygen-free environments in loess-paleosol sediments, and Ohmoto (2003) and Otake et al. (2007) even describe non-redox transformations between magnetite and hematite under H_2-rich hydrothermal conditions, a mechanism that is not only restricted to Earth's surface but that can also act at greater depths in the crust. These interpretations have been used to explain irreversibility of κ-T experiments in impact studies (e.g., Mang & Kontny, 2013).

Mendes et al. (2023) postulated that in shocked magnetite from the peak ring of the Chicxulub impact structure, natural hydrothermal temperatures are insufficient to cause annealing or hem-mt transformation. We confirm this interpretation with our results, as the preservation of both the shocked and oxidized state (see RT results from sample 1,100 in Figures 3, 4c and 7b), suggests that even long exposures (from 500 Kyr to 2 Myr) to relatively

high hydrothermal temperatures of 450°C (Kring et al., 2020) is insufficient to initiate such a process. Because magnetite already shows signs of annealing when heated to 540°C, we place the temperature threshold for the initiation of annealing between 450° and 540°C. The results of the Soultz 2,533 sample from this study suggest that most of the hem-mt transformation occurs above 560°C and the bulk of new magnetite formation occurs above 600°C. No transformation is observed below the Curie temperature of magnetite (~580°C) in the κ-T curves of Soultz (Figure 1d), so we estimate that ~580°C is a reasonable threshold for the onset of the hem-mt transformation in most samples.

Several geoscience research subjects report hem-mt transformation at high temperatures: from impact research, loess deposit research, to environmental contamination studies and wildfire related mineral transformations in soils (e.g., Deng et al., 2001; Górka-Kostrubiec et al., 2019; Jiang et al., 2016; Just & Kontny, 2012; Mang & Kontny, 2013; Szczepaniak-Wnuk et al., 2020). Oches and Banerjee (1996) hypothesized about high-temperature hem-mt transformation in κ-T analyses, but to our knowledge no in-depth study of this phenomenon has been published. Despite the pre-impact oxidation being ubiquitous in the Chicxulub peak-ring (Kring et al., 2020), wherever the granite is in proximity to the impact melt hematite is absent and κ-T curves become more reversible, or show the "hump" also before heating (Mendes et al., 2023). This suggests that the hem-mt transformation is not exclusively related to an argon atmosphere with traces of hydrocarbons, but can also occur in nature under reducing high-temperature conditions, for example, related to a magmatic pulse (e.g., through orogenic re-burial, dyke emplacement, or sequential plutonic emplacement).

A potential case study for a possible unnoticed overprint of natural hem-mt transformation is the Manteigas granodiorite, in central Portugal (Dias et al., 2022). This is a Lower Ordovician granodiorite (481.1 ± 5.9 ma; Neiva et al., 2009), and was intruded by the adjacent Seia granite in the late Carboniferous (311-306 Ma; Santʼ Ovaia et al., 2010). Dias et al. (2022) described the presence of large (>100 μm) magnetite crystals, that are partially oxidized into hematite. IRM modeling for these samples indicate that, where only magnetite is identified, B_h ranges from 25 to 40 mT. However, close to the contact with the younger Seia pluton, some hematite is observed (~15% contribution to the signal), and the magnetite component coercivity is higher (60–63 mT). This coercivity difference is similar to the observed increases in our results, attributed to the hem-mt transformation, even when incomplete (see e.g., Sample 2,533 in Table 1; Table 2). If partial hem-mt transformation occurred in the granodiorite due to the emplacement of the Seia granite, this may have led to incorrect conclusions. It would be difficult to identify a hem-mt derived overprint without looking for it. Our results demonstrate that formation of small-scale SD-SP state grains overprint original magnetic signals and increases magnetizations (e.g., Figure 7a). SD grains are more stable and reliable recorders of paleomagnetic directions than MD grains at a geological time-scale (e.g., Heider et al., 1988; Roberts et al., 2017), therefore, even a small fraction of SD grains formed by the hem-mt transformation provides a mechanism for overprinting paleomagnetic recordings. We believe that hem-mt transformation may be an under-appreciated mechanism that deserves more attention in future studies.

5. Conclusions

Using FORC measurements to detect subtle magnetic behavior and domain state variations, we have characterized how shock, annealing, oxidation and hematite-to-magnetite transformation produce different magnetic behavior responses with temperature. We demonstrate that shock pressures above the Hugoniot elastic limit for magnetite (~5 GPa) have a tangible effect on the apparent domain state of magnetite, causing MD grains to behave PSD/MV-like, despite maintaining multiple discrete domains. Brittle fracturing and grain fragmentation are irreversible, and cause permanent grain size reduction with a bulk-sample average domain state decrease, creating "real" MV state grains. On the other hand, thermal annealing of strained magnetite recovers some of the lattice defects by grain recrystallization and lattice defect recovery. The reduction of intra-crystalline strain and defect networks reduces domain wall pinning, and partially restores some of the original MD behavior. Together, these mechanisms cause a bulk-sample increased domain state, with a composite MD and (real) MV magnetic behavior, after heating. The temperature threshold for annealing is estimated to be between ca. ~500–520°C.

High temperature hematite-to-magnetite transformation in a non-oxidizing argon atmosphere caused the formation of SD-SP magnetite and a bulk-sample average domain state decrease. Even in small amounts, the newly formed SD magnetite causes a strong magnetic signal increase that overprints the original signal, and masks any thermal annealing effect, making hem-mt transformation the dominant phenomenon of the two. The new SD-SP

phase is stable and the transformation irreversible, even after consecutive heating. We estimate transformation to initiate at ~580°C, becoming most prominent above 600°C. Formation of new SD magnetite as a response to temperature may overprint paleomagnetic directions and other magnetic behaviors in nature, creating the need for an extra layer of scrutiny when interpreting paleomagnetic data. It may also be a new process for producing remagnetizations.

Data Availability Statement

The data used for this study are available at Mendes and Kontny (2023) [Dataset], and consist of hysteresis, direct current demagnetization (DCD) and first order reversal curves (FORC), all in single ".vres" data files for each temperature step of each sample. All files, as well as extra diagrams are available under the name of "supplemental files" as referred to in the text, in the Mendeley Data repository, DOI: 10.17632/f66zx5bjnp.2. We used the free software ImageJ (Rasband, 1997) for SD-MD area calculations, available for Download (nih.gov); or in-browser at ImageJ.JS(imjoy.io) We processed our data using the MAX Unmix software (Maxbauer et al., 2016) a free web application software available at shinyapps.its.carleton.edu/max-unmix/. We used FORCinel (ver.3.08; Harrison & Feinberg, 2008) to process FORC data. This is a free software available at https://nanopaleomag.esc.cam.ac.uk/nanopaleomag-home/forcinel/download/, and requires the Igor Pro (ver 9.0) software package, created and distributed by WaveMetrics, available at https://www.wavemetrics.com/support/demos. The "Pro" version is only available for free as a Demo for 30 days, after which some limitations are imposed on a free user but do not inhibit the processing in any meaningful capacity. No registration is required to acquire our data, or any of the software used.

Acknowledgments

BDLM thanks Dr. Maxwell Brown, Dr. Peter Solheid, and academic staff at IRM Minneapolis for their assistance in the laboratory. Part of this work was performed as a Visiting Fellow at the Institute for Rock Magnetism (IRM) at the University of Minnesota. The IRM is a US National Multi-User Facility supported through the Instrumentation and Facilities program of the National Science Foundation, Earth Sciences Division (NSF EAR-2153786), and by funding from the University of Minnesota. This work was funded by the German Research Foundation, project number 432762445, and partially supported by the Institute for Rock Magnetism (IRM), Minneapolis, USA, through a Visiting Research Fellowship. We acknowledge the thorough reviews by Bjarne Almqvist, Andrew Roberts and two anonymous reviewers. Open Access funding enabled and organized by Projekt DEAL.

References

Ahrens, T. J., & Johnson, M. L. (1995). Shock wave data for rocks. *Mineral Physics and Crystallography, A Handbook of Physical Constants*, *3*, 35–44.

Annersten, H., & Hafner, S. S. (1973). Vacancy distribution in synthetic spinels of the series Fe_3O_4—γ-Fe_2O_3. *Zeitschrift Fur Kristallographie - New Crystal Structures*, *137*(5–6), 321–340. https://doi.org/10.1524/zkri.1973.137.5-6.321

Barkhausen, H. (1919). *Physikalische Zeitschrift*, *20*, 401.

Birčáková, Z., Kollár, P., Jakubčin, M., Füzer, J., Bureš, R., & Fáberová, M. (2019). Reversible and irreversible magnetization processes along DC hysteresis loops of Fe-based composite materials. *Journal of Magnetism and Magnetic Materials*, *483*, 183–190. https://doi.org/10.1016/j.jmmm.2019.03.115

Carporzen, L., & Gilder, S. A. (2010). Strain memory of the Verwey transition. *Journal of Geophysical Research*, *115*(B5), 5103. https://doi.org/10.1029/2009JB006813

Carporzen, L., Gilder, S. A., & Hart, R. J. (2006). Origin and implications of two Verwey transitions in the basement rocks of the Vredefort meteorite crater, South Africa. *Earth and Planetary Science Letters*, *251*(3–4), 305–317. https://doi.org/10.1016/j.epsl.2006.09.013

Day, R., Fuller, M., & Schmidt, V. A. (1977). Hysteresis properties of titanomagnetites: Grain-size and compositional dependence. *Physics of the Earth and Planetary Interiors*, *13*(4), 260–267. https://doi.org/10.1016/0031-9201(77)90108-X

Deng, C., Zhu, R., Jackson, M. J., Verosub, K. L., & Singer, M. J. (2001). Variability of the temperature-dependent susceptibility of the Holocene eolian deposits in the Chinese loess plateau: A pedogenesis indicator. *Physics and Chemistry of the Earth - Part A: Solid Earth and Geodesy*, *26*(11–12), 873–878. https://doi.org/10.1016/S1464-1895(01)00135-1

Dias, J. M., Cruz, C., Sant'ovaia, H., & Noronha, F. (2022). Assessing the magnetic mineralogy of the pre-Variscan Manteigas granodiorite: An unexpected case of a magnetite-series granitoid in Portugal. *Minerals*, *12*(4), 440. https://doi.org/10.3390/MIN12040440

Dunlop, D. J. (1973). Superparamagnetic and single-domain threshold sizes in magnetite. *Journal of Geophysical Research*, *78*(11), 1780–1793. https://doi.org/10.1029/JB078i011p01780

Dunlop, D. J. (2014). High-temperature susceptibility of magnetite: A new pseudo-single-domain effect. *Geophysical Journal International*, *199*(2), 707–716. https://doi.org/10.1093/GJI/GGU247

Egli, R. (2021). Magnetic characterization of geologic materials with first-order reversal curves. *Magnetic measurement techniques for materials characterization*, 455–604. https://doi.org/10.1007/978-3-030-70443-8_17

Feignon, J. G., FerriÈre, L., Leroux, H., & Koeberl, C. (2020). Characterization of shocked quartz grains from Chicxulub peak ring granites and shock pressure estimates. *Meteoritics & Planetary Sciences*, *55*(10), 2206–2223. https://doi.org/10.1111/maps.13570

Frank, U., & Nowaczyk, N. R. (2008). Mineral magnetic properties of artificial samples systematically mixed from haematite and magnetite. *Geophysical Journal International*, *175*(2), 449–461. https://doi.org/10.1111/j.1365-246X.2008.03821.x

Fritz, J., Wünnemann, K., Reimold, W. U., Meyer, C., & Hornemann, U. (2011). Shock experiments on quartz targets pre-cooled to 77 K. *International Journal of Impact Engineering*, *38*(6), 440–445. https://doi.org/10.1016/j.ijimpeng.2010.10.014

Gao, X., Hao, Q., Oldfield, F., Bloemendal, J., Deng, C., Wang, L., et al. (2019). New high-temperature dependence of magnetic susceptibility-based climofunction for quantifying paleoprecipitation from Chinese Loess. *Geochemistry, Geophysics, Geosystems*, *20*(8), 4273–4291. https://doi.org/10.1029/2019GC008401

Gattacceca, J., Lamali, A., Rochette, P., Boustie, M., & Berthe, L. (2007). The effects of explosive-driven shocks on the natural remanent magnetization and the magnetic properties of rocks. *Physics of the Earth and Planetary Interiors*, *162*(1–2), 85–98. https://doi.org/10.1016/J.PEPI.2007.03.006

Gilder, S. A., Goff, M. L., & Chervin, J. C. (2006). Static stress demagnetization of single and multidomain magnetite with implications for meteorite impacts. *High Pressure Research*, *26*(4), 539–547. https://doi.org/10.1080/08957950601092085

Gilder, S. A., LeGoff, M., Chervin, J. C., & Peyronneau, J. (2004). Magnetic properties of single and multi-domain magnetite under pressures from 0 to 6 GPa. *Geophysical Research Letters*, *31*(10). https://doi.org/10.1029/2004GL019844

Gilder, S. A., LeGoff, M., Peyronneau, J., & Chervin, J. C. (2002). Novel high pressure magnetic measurements with application to magnetite. *Geophysical Research Letters*, *29*(10), 30–31. https://doi.org/10.1029/2001GL014227

Gilder, S. A., Pohl, J., & Eitel, M. (2018). Magnetic signatures of terrestrial meteorit. *Impact Craters: A Summary*, 357–382. https://doi.org/10.1007/978-3-319-64292-5_13

Górka-Kostrubiec, B., Werner, T., Dytłow, S., Szczepaniak-Wnuk, I., Jeleńska, M., & Hanc-Kuczkowska, A. (2019). Detection of metallic iron in urban dust by using high-temperature measurements supplemented with microscopic observations and Mössbauer spectra. *Journal of Applied Geophysics*, *166*, 89–102. https://doi.org/10.1016/J.JAPPGEO.2019.04.022

Harrison, R. J., & Feinberg, J. M. (2008). FORCinel: An improved algorithm for calculating first-order reversal curve distributions using locally weighted regression smoothing. [Software]. Geochemistry, Geophysics, Geosystems, *9*, 5. https://doi.org/10.1029/2008GC001987

Harrison, R. J., Muraszko, J., Heslop, D., Lascu, I., Muxworthy, A. R., & Roberts, A. P. (2018). An improved algorithm for unmixing first-order reversal curve diagrams using principal component analysis. *Geochemistry, Geophysics, Geosystems*, *19*(5), 1595–1610. https://doi.org/10.1029/2018GC007511

Hart, R. J., Hargraves, R. B., Andreoli, M. A. G., Tredoux, M., & Doucouré, C. M. (1995). Magnetic anomaly near the center of the Vredefort structure: Implications for impact-related magnetic signatures. *Geology*, *23*(3), 277–280. https://doi.org/10.1130/0091-7613(1995)023%3C0277:MANTCO%3E2.3.CO;2

Heider, F., Halgedahl, S. L., & Dunlop, D. J. (1988). Temperature dependence of magnetic domains in magnetite crystals. *Geophysical Research Letters*, *15*(5), 499–502. https://doi.org/10.1029/GL015i005p00499

Heslop, D., McIntosh, G., & Dekkers, M. J. (2004). Using time- and temperature-dependent Preisach models to investigate the limitations of modelling isothermal remanent magnetization acquisition curves with cumulative log Gaussian functions. *Geophysical Journal International*, *157*(1), 55–63. https://doi.org/10.1111/j.1365-246X.2004.02155.x

Heslop, D., & Roberts, A. P. (2012). A method for unmixing magnetic hysteresis loops. *Journal of Geophysical Research*, *117*(B3). https://doi.org/10.1029/2011JB008859

Hildebrand, A. R., Penfield, G. T., Kring, D. A., Pilkington, M., Camargo, Z. A., Jacobsen, S. B., & Boynton, W. V. (1991). Chicxulub crater: A possible cretaceous/tertiary boundary impact crater on the Yucatan Peninsula, Mexico. *Geology*, *19*(9), 867–871. https://doi.org/10.1130/0091-7613(1991)019<0867:CCAPCT>2.3.CO;2

Hopkinson, J. (1889). XIV. Magnetic and other physical properties of iron at a high temperature. *Philosophical Transactions of the Royal Society of London - A*(180), 443–465. https://doi.org/10.1098/rsta.1889.0014

Horton, J. W., Jr., Gibson, R. L., Reimold, W. U., Wittmann, A., Gohn, G. S., & Edwards, L. E. (2009). Geologic columns for the ICDP-USGS Eyreville B core, Chesapeake Bay impact structure: Impactites and crystalline rocks, 1766 to 1096 m depth. *Geological Society of America Special Paper*, *458*, 21–49.

Horton, J. W., Jr., Kunk, M. J., Belkin, H. E., Aleinikoff, J. N., Jackson, J. C., & Chou, I. M. (2009). Evolution of crystalline target rocks and impactites in the Chesapeake Bay impact structure, ICDP-USGS Eyreville B core. *Geological Society of America Special Paper*, *458*, 277–316.

Horton, J. W., Vanko, D. A., Naeser, C. W., Naeser, N. D., Larsen, D., Jackson, J. C., & Belkin, H. E. (2006). Postimpact hydrothermal conditions at the central uplift, Chesapeake Bay impact structure, Virginia, USA. *LPI*, *956*, 1842. Retrived from https://ui.adsabs.harvard.edu/abs/2006LPI.37.1842H/abstract

Jiang, Z., Liu, Q., Zhao, X., Roberts, A. P., Heslop, D., Barrón, V., & Torrent, J. (2016). Magnetism of Al-substituted magnetite reduced from Al-hematite. *Journal of Geophysical Research: Solid Earth*, *121*(6), 4195–4210. https://doi.org/10.1002/2016JB012863

Just, J., & Kontny, A. (2012). Thermally induced alterations of minerals during measurements of the temperature dependence of magnetic susceptibility: A case study from the hydrothermally altered Soultz-sous-Forêts granite, France. *International Journal of Earth Sciences*, *101*(3), 819–839. https://doi.org/10.1007/s00531-011-0668-9

Kontny, A., Elbra, T., Just, J., Pesonen, L. J., Schleicher, A. M., & Zolk, J. (2007). Petrography and shock-related remagnetization of pyrrhotite in drill cores from the Bosumtwi impact crater drilling project, Ghana. *Meteoritics & Planetary Sciences*, *42*(4–5), 811–827. https://doi.org/10.1111/J.1945-5100.2007.TB01077.X

Kontny, A., Reznik, B., Boubnov, A., Göttlicher, J., & Steininger, R. (2018). Postshock thermally induced transformations in experimentally shocked magnetite. *Geochemistry, Geophysics, Geosystems*, *19*(3), 921–931. https://doi.org/10.1002/2017GC007331

Kring, D. A., Tikoo, S. M., Schmieder, M., Riller, U., Rebolledo-Vieyra, M., Simpson, S. L., et al. (2020). Probing the hydrothermal system of the Chicxulub impact crater. *Science Advances*, *6*(22), 3053–3082. https://doi.org/10.1126/sciadv.aaz3053

Lascu, I., Einsle, J. F., Ball, M. R., & Harrison, R. J. (2018). The vortex state in geologic materials: A micromagnetic perspective. *Journal of Geophysical Research: Solid Earth*, *123*(9), 7285–7304. https://doi.org/10.1029/2018JB015909

Lindquist, A. K., Feinberg, J. M., Harrison, R. J., Loudon, J. C., & Newell, A. J. (2015). Domain wall pinning and dislocations: Investigating magnetite deformed under conditions analogous to nature using transmission electron microscopy. *Journal of Geophysical Research: Solid Earth*, *120*(3), 1415–1430. https://doi.org/10.1002/2014JB011335

Liu, P., Hirt, A. M., Schüler, D., Uebe, R., Zhu, P., Liu, T., & Zhang, H. (2019). Numerical unmixing of weakly and strongly magnetic minerals: Examples with synthetic mixtures of magnetite and hematite. *Geophysical Journal International*, *217*(1), 280–287. https://doi.org/10.1093/gji/ggz022

Louzada, K. L., Stewart, S. T., Weiss, B. P., Gattacceca, J., & Bezaeva, N. S. (2010). Shock and static pressure demagnetization of pyrrhotite and implications for the Martian crust. *Earth and Planetary Science Letters*, *290*(1–2), 90–101. https://doi.org/10.1016/j.epsl.2009.12.006

Mang, C., & Kontny, A. (2013). Origin of two Verwey transitions in different generations of magnetite from the Chesapeake Bay impact structure, USA. *Journal of Geophysical Research: Solid Earth*, *118*(10), 5195–5207. https://doi.org/10.1002/JGRB.50291

Maxbauer, D. P., Feinberg, J. M., & Fox, D. L. (2016). MAX UnMix: A web application for unmixing magnetic coercivity distributions [Software]. Computers and Geosciences, *95*, 140–145. https://doi.org/10.1016/j.cageo.2016.07.009

Mendes, B., & Kontny, A. (2023). Restoration and transformation: The response of shocked and oxidized magnetite to temperature [Dataset]. Mendeley Data, *2*. https://doi.org/10.17632/f66zx5bjnp.2

Mendes, B. D. L., Kontny, A., Polchau, M., Fischer, L. A., Gaus, K., Dudzisz, K., & Dekkers, M. J. (2023). Peak-ring magnetism: Rock and mineral magnetic properties of the Chicxulub impact crater. *The Geological Society of America Bulletin*. https://doi.org/10.1130/B36547.1

Morgan, J., Gulick, S., Mellett, C. L., & Green, S. L. (2017). Chicxulub: Drilling the K-Pg impact crater. *Proceedings of the International Ocean Discovery Program*, *364*. https://doi.org/10.14379/IODP.PROC.364.2017

Morris, R. V., Golden, D. C., Bell, J. F., & Lauer, H. V. (1995). Hematite, pyroxene, and phyllosilicates on Mars: Implications from oxidized impact melt rocks from Manicouagan Crater, Quebec, Canada. *Journal of Geophysical Research*, *100*(E3), 5319–5328. https://doi.org/10.1029/94JE01500

Morris, R. V., Klingelhöfer, G., Schröder, C., Rodionov, D. S., Yen, A., Ming, D. W., et al. (2006). Mössbauer mineralogy of rock, soil, and dust at Gusev crater, Mars: Spirit's journey through weakly altered olivine basalt on the plains and pervasively altered basalt in the Columbia Hills. *Journal of Geophysical Research*, *111*(E2). https://doi.org/10.1029/2005JE002584

Moskowitz, B. M. (1993). Micromagnetic study of the influence of crystal defects on coercivity in magnetite. *Journal of Geophysical Research*, *98*(B10), 18011–18026. https://doi.org/10.1029/93JB01719

Müller, W. F., & Hornemann, U. (1969). Shock-induced planar deformation structures in experimentally shock-loaded olivines and in olivines from chondritic meteorites. *Earth and Planetary Science Letters*, *7*(3), 251–264. https://doi.org/10.1016/0012-821X(69)90062-4

Nagy, L., Williams, W., Tauxe, L., & Muxworthy, A. R. (2019). From nano to micro: Evolution of magnetic domain structures in multidomain magnetite. *Geochemistry, Geophysics, Geosystems*, *20*(6), 2907–2918. https://doi.org/10.1029/2019GC008319

Neiva, A. M. R., Williams, I. S., Ramos, J. M. F., Gomes, M. E. P., Silva, M. M. V. G., & Antunes, I. M. H. R. (2009). Geochemical and isotopic constraints on the petrogenesis of Early Ordovician granodiorite and Variscan two-mica granites from the Gouveia area, central Portugal. *Lithos*, *111*(3–4), 186–202. https://doi.org/10.1016/J.LITHOS.2009.01.005

Newell, A. J., & Merrill, R. T. (1999). Single-domain critical sizes for coercivity and remanence. *Journal of Geophysical Research*, *104*(B1), 617–628. https://doi.org/10.1029/1998JB900039

Oches, E. A., & Banerjee, S. K. (1996). Rock-magnetic proxies of climate change from loess-paleosol sediments of the Czech Republic. *Studia Geophysica et Geodaetica*, *40*(3), 287–300. https://doi.org/10.1007/BF02300744

Ohmoto, H. (2003). Nonredox transformations of magnetite-hematite in hydrothermal systems. *Economic Geology*, *98*(1), 157–161. https://doi.org/10.2113/gsecongeo.98.1.157

Otake, T., Wesolowski, D. J., Anovitz, L. M., Allard, L. F., & Ohmoto, H. (2007). Experimental evidence for non-redox transformations between magnetite and hematite under H2-rich hydrothermal conditions. *Earth and Planetary Science Letters*, *257*(1–2), 60–70. https://doi.org/10.1016/j.epsl.2007.02.022

Özdemir, Ö., & Dunlop, D. J. (1997). Effect of crystal defects and internal stress on the domain structure and magnetic properties of magnetite. *Journal of Geophysical Research*, *102*(B9), 20211–20224. https://doi.org/10.1029/97JB01779

Penfield, G. T., & Camargo, A. (1981). Definition of a major igneous zone in the central Yucatán platform with aeromagnetics and gravity [abs.]. In *51st annual meet-ing of the society of exploration geophysicists* (p. 37). Society of Exploration Geophysicists.

Pike, C., & Fernandez, A. (1999). An investigation of magnetic reversal in submicron-scale Co dots using first order reversal curve diagrams. *Journal of Applied Physics*, *85*(9), 6668–6676. https://doi.org/10.1063/1.370177

Pike, C. R. (2003). First-order reversal-curve diagrams and reversible magnetization. *Physical Review B*, *68*(10), 104424. https://doi.org/10.1103/PhysRevB.68.104424

Pike, C. R., Roberts, A. P., Dekkers, M. J., & Verosub, K. L. (2001). An investigation of multi-domain hysteresis mechanisms using FORC diagrams. *Physics of the Earth and Planetary Interiors*, *126*(1–2), 11–25. https://doi.org/10.1016/S0031-9201(01)00241-2

Pike, C. R., Roberts, A. P., & Verosub, K. L. (1999). Characterizing interactions in fine magnetic particle systems using first order reversal curves. *Journal of Applied Physics*, *85*(9), 6660–6667. https://doi.org/10.1063/1.370176

Pike, C. R., Roberts, A. P., & Verosub, K. L. (2001). First order reversal curve diagrams and thermal relaxation effects in magnetic particles. *Geophysical Journal International*, *145*(3), 721–730. https://doi.org/10.1046/j.0956-540x.2001.01419.x

Pilkington, M., & Grieve, R. A. F. (1992). The geophysical signature of terrestrial impact craters. *Reviews of Geophysics*, *30*(2), 161–181. https://doi.org/10.1029/92RG00192

Plado, J., Pesonen, L., & Puura, V. (1999). Effect of erosion on gravity and magnetic signatures of complex impact structures: Geophysical modeling and applications. *Geological Society of America*, 229–240.

Quesnel, Y., Gattacceca, J. Ô., Osinski, G. R., & Rochette, P. (2013). Origin of the central magnetic anomaly at the Haughton impact structure, Canada. *Earth and Planetary Science Letters*, *367*, 116–122. https://doi.org/10.1016/J.EPSL.2013.02.032

Rasband, W. S. (1997). ImageJ [Software]. US National Institutes of Health. Retrieved from https://imagej.net/ij/

Reznik, B., Kontny, A., Fritz, J., & Gerhards, U. (2016). Shock-induced deformation phenomena in magnetite and their consequences on magnetic properties. *Geochemistry, Geophysics, Geosystems*, *17*(6), 2374–2393. https://doi.org/10.1002/2016GC006338

Roberts, A. P., Almeida, T. P., Church, N. S., Harrison, R. J., Heslop, D., Li, Y., et al. (2017). Resolving the Origin of pseudo-single domain magnetic behavior. *Journal of Geophysical Research: Solid Earth*, *122*(12), 9534–9558. https://doi.org/10.1002/2017JB014860

Roberts, A. P., Heslop, D., Zhao, X., & Pike, C. R. (2014). Understanding fine magnetic particle systems through use of first-order reversal curve diagrams. *Reviews of Geophysics*, *52*(4), 557–602. https://doi.org/10.1002/2014RG000462

Roberts, A. P., Hu, P., Harrison, R. J., Heslop, D., Muxworthy, A. R., Oda, H., et al. (2019). Domain state diagnosis in rock magnetism: Evaluation of potential alternatives to the Day diagram. *Journal of Geophysical Research: Solid Earth*, *124*(6), 5286–5314. https://doi.org/10.1029/2018JB017049

Roberts, A. P., Pike, C. R., & Verosub, K. L. (2000). First-order reversal curve diagrams: A new tool for characterizing the magnetic properties of natural samples. *Journal of Geophysical Research*, *105*(B12), 28461–28475. https://doi.org/10.1029/2000JB900326

Robertson, D. J., & France, D. E. (1994). Discrimination of remanence-carrying minerals in mixtures, using isothermal remanent magnetisation acquisition curves. *Physics of the Earth and Planetary Interiors*, *82*(3–4), 223–234. https://doi.org/10.1016/0031-9201(94)90074-4

Sant'Ovaia, H., Olivier, P., Ferreira, N., Noronha, F., & Leblanc, D. (2010). Magmatic structures and kinematics emplacement of the Variscan granites from Central Portugal (Serra da Estrela and Castro Daire areas). *Journal of Structural Geology*, *32*(10), 1450–1465. https://doi.org/10.1016/J.JSG.2010.09.003

Schulte, P., Alegret, L., Arenillas, I., Arz, J. A., Barton, P. J., Bown, P. R., et al. (2010). The chicxulub asteroid impact and mass extinction at the cretaceous-paleogene boundary. *Science*, *327*(5970), 1214–1218. https://doi.org/10.1126/SCIENCE.1177265

Scott, R. G., Pilkington, M., Tanczyk, E. I., & Grieve, R. A. F. (1995). Magnetic properties of three impact structures in Canada. *Meteoritics*, *30*.

Sergienko, E. S., Yanson, S. Y., Kosterov, A., Kharitonskii, P. V., & Frolov, A. M. (2021). Suevites and tagamites of Zhamanshin Astrobleme: Distribution in the crater and petrographic features. *IOP Conference Series: Earth and Environmental Science*, *666*(4), 042080. https://doi.org/10.1088/1755-1315/666/4/042080

Sharpton, V. L., Brent Dalrymple, G., Marín, L. E., Ryder, G., Schuraytz, B. C., & Urrutia-Fucugauchi, J. (1992). New links between the Chicxulub impact structure and the Cretaceous/Tertiary boundary. *Nature*, *359*(6398), 819–821. https://doi.org/10.1038/359819a0

Smit, J. (1999). The global stratigraphy of the Cretaceous-Tertiary boundary impact ejecta. *Annual Review of Earth and Planetary Sciences*, *27*(1), 75–113. https://doi.org/10.1146/annurev.earth.27.1.75

Szczepaniak-Wnuk, I., Górka-Kostrubiec, B., Dytłow, S., Szwarczewski, P., Kwapuliński, P., & Karasiński, J. (2020). Assessment of heavy metal pollution in Vistula river (Poland) sediments by using magnetic methods. https://doi.org/10.1007/s11356-020-08608-4

Tikoo, S. M., Gattacceca, J., Swanson-Hysell, N. L., Weiss, B. P., Suavet, C., & Cournède, C. (2015). Preservation and detectability of shock-induced magnetization. *Journal of Geophysical Research: Planets*, *120*(9), 1461–1475. https://doi.org/10.1002/2015JE004840

Witt, A., Fabian, K., & Bleil, U. (2005). Three-dimensional micromagnetic calculations for naturally shaped magnetite: Octahedra and magnetosomes. *Earth and Planetary Science Letters*, *233*(3–4), 311–324. https://doi.org/10.1016/j.epsl.2005.01.043

Zhao, X., Roberts, A. P., Heslop, D., Paterson, G. A., Li, Y., & Li, J. (2017). Magnetic domain state diagnosis using hysteresis reversal curves. *Journal of Geophysical Research: Solid Earth*, *122*(7), 4767–4789. https://doi.org/10.1002/2016JB013683

Zhao, X. Y., & Liu, Q. S. (2010). Effects of the grain size distribution on the temperature-dependent magnetic susceptibility of magnetite nanoparticles. *Science China Earth Sciences*, *53*(7), 1071–1078. https://doi.org/10.1007/s11430-010-4015-y